ETH
Eidgenössische Technische Hochschule Zürich
Swiss Federal Institute of Technology Zurich

MASTER THESIS

Characterization of Overcoupled NbTiN Microwave Resonators up to 40 GHz

Raphael Barmettler
2011/2012

Supervisor
Tobias Thiele
Andreas Wallraff

Abstract

In this master thesis overcoupled superconducting NbTiN microwave resonators on chips are characterized. We are interested in measuring and simulating the Q-factors, the coupling capacitance and the propagation constant for different chip designs. To achieve this goal, we increase the complexity of the chip design from a straight to a curved transmission line with different resonator lengthes. Every chip is made at least twice for testing the reproducibility of the measurements. Finally, we analyze the kinetic induction in NbTiN for different chip temperatures from 8 to 13 K and for different chip geometries. These measurements are an important step towards a hybrid system at 4 K, where Rydberg atoms couple to chip-based microwave photons.

Contents

Chapter 1

Introduction

1.1 Quantum Computation

In our daily life we are surrounded by computers and other similar electronic equipment without modern life was unthinkable. The main ingredient of every such device is called transistor and its number defines the computational power. A transistor consists of doped semiconductors and can be in two different states, namely 1 (current flows through the transistor) or 0 (no or low current flows through the transistor). Such a device has therefore the perfect properties to be used as a bit (binary digits). A bit is the smallest unit of information, which is encoded here as the distinction of the two states of a transistor. Today the RAM, processors and the memory of a modern computer mainly consists of billions of transistors, which is the most successful system for a classical bit.

Moore's law tells us, that the number of transistor per unit area doubles every two years. Thus the transistor has to become smaller and smaller. Since on scale of few nanometers the quantum nature of the transistor becomes important, one could think of using its properties to create a more powerful computer, a quantum computer. A quantum computer would differ from a classical computer in its most basic element, the bit.

In a quantum computer the bits are replaced by qubits, which consist of two different energy states, called $|0\rangle$ and $|1\rangle$ similar to a classical computer, but with the difference, that the qubit state can also be in superposition of these two so called computational states:

$$|\psi\rangle = \alpha|0\rangle + \beta|1\rangle, \tag{1.1}$$

where $||\alpha||^2 + ||\beta||^2 = 1$ and $\alpha, \beta \in \mathbb{C}$.

Since two complex numbers have four degrees of freedom, with the normalization of α and β and an arbitrary global phase two degrees of freedom

remain to choose for α and β. Therefore every state of a two level system (TLS) can be represented on the surface of a sphere, the Bloch sphere, the states $|0\rangle$ and $|1\rangle$ lie on the poles and all equal superpositions with some phase on the equator.

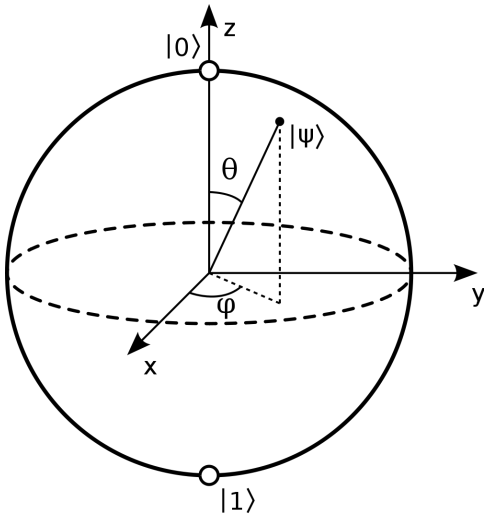

Figure 1.1: The representation of the state of a qubit as a vector on the Bloch sphere. The angles θ and φ are defined by $\alpha = \cos\frac{\theta}{2}$ and $\beta = e^{i\varphi}\sin\frac{\theta}{2}$. [1]

If two (or more) qubits are part of a system, the basis states are given by the tensor product of the computational basis of every qubit. In general the state of the system is a superposition of these basis states.

$$|\psi\rangle = \alpha|0\rangle|0\rangle + \beta|1\rangle|0\rangle + \gamma|0\rangle|1\rangle + \delta|1\rangle|1\rangle, \tag{1.2}$$

Some of this superposition states are not tensor products of single qubit states and can therefore not be seen as two separated states. These states are called entangled. An example for a entangled state is the bell state $|\psi\rangle = \frac{1}{\sqrt{2}}(|0\rangle|0\rangle + |1\rangle|1\rangle)$.

Obviously a qubit is a generalization of a classical bit. This means every classical algorithm can be implemented on a quantum computer. The major advantage of a quantum computer over a classical computer is due to entangled state. In quantum computation the input is saved in the state of the qubits at the beginning of the calculation. Then different gates are applied, which change these states and entangle different qubits. At the end of the calculation the states of the qubit are measured and give the result of the calculation. Typical improvement of quantum algorithm over classical algorithm are expected to be factorizing prime numbers (Shor's algorithm) and searching a data base (Grover's algorithm) more efficient. The Shor's

algorithm finish the factorization in polynomial time, while the algorithms of a classical computer runs at least in sub-exponential time [2]. In models of classical computation, searching an unsorted database cannot be done in less than linear time, but Grover's algorithm illustrates that with quantum computation searching can be done in $O(\sqrt{N})$ [3]. Also simulation of complicated quantum system can be done faster on a quantum computer.

In theory, every quantum mechanical two level system can be used as a qubit. Anyhow today it is not clear, if and which of the numerous ideas for qubits and quantum computers will be as successful as the transistor. The most promising candidates nowadays are cavity QED, trapped Ions, quantum dots and NMR. They all suffer from two problems, decoherence and scalability. Decoherence is the loss of quantum information before the calculation has finished. For example, if the excited state decays to its ground state. The scalability is the ability to fabricate a lot of identical qubits at the same time while maintaining individual control and addressability for each is a substantial prerequisite. A possible solution for the decoherence might be hybrid systems, where two different sorts of qubits with different coherence time are used. One qubit with a shorter coherence time is used to calculate (processor), while another qubit with a longer coherence time is used as RAM. More information about hybrid system can be found in section 2.3.

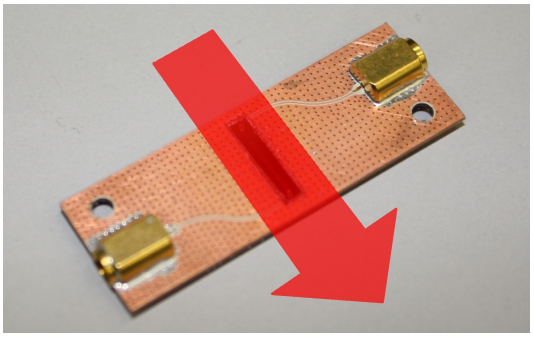

Figure 1.2: Schematic sketch of the hybrid system. The Rydberg atoms (represented by the red arrow) fly a up to millimeter over the resonator and couple to the microwave photons.

The experiment, where this master thesis contributes, tries to join circuit QED (section 2.2), as part of cavity QED (section 2.1), and Rydberg atoms (section 2.3.1) to a hybrid system (section2.3). The Rydberg atoms fly over a chip surface (Fig. 1.2) and couple to microwave photons in a waveguide (section 2.4) on the chip. The goal of this master thesis is to characterize

the transmission and reflexion spectrum of a superconducting waveguide resonator on the chip. This was done in previous experiments with a waveguide consisting of Nb on sapphire. In this experiment we use NbTiN on sapphire waveguides and characterize their spectra. The new material is expected to raise the internal quality factors of the resonators (section 2.4).

Chapter 2

Theory

2.1 Cavity QED

The idea of Cavity QED as an architecture for a quantum computer is based on interfacing stationary qubits, such as ground state of atoms, with flying qubits such as photons. Since the interactions between the atoms and the photons is very weak in free space, putting atoms in a cavity allows to enhance their coupling [4].

Quantum electrodynamic (QED) describe the phenomena of light quantum mechanically. In free space the modes of the photons are continuous distributed. But if there are boundary conditions, for example in a cavity, there is only discrete set of allowed modes with frequencies ω_r (cavity QED). A famous Hamiltonian in cQED, the Jaynes-Cummings Hamiltonian, describes a single field mode coupled to a quantum mechanical two level system (TLS): [5]

$$H = \hbar\omega_r(a^\dagger a + \frac{1}{2}) + \frac{\hbar\Omega}{2}\sigma^z + \hbar g(a^\dagger\sigma^- + a\sigma^+) + H_\kappa + H_\gamma, \tag{2.1}$$

The first term is the Hamiltonian of the photons in a cavity mode, where $a^\dagger$ and a are the creation and the annihilation operator of a photon and ω_r is the cavity resonance frequency. The second term of Eq. 2.1 is the Hamiltonian of the TLS, where Ω is its frequency and σ^z is a Pauli matrix. The third term describes the coupling between the two systems, where a creation (annihilation) of a photon needs a decay (excitation) of the TLS. The state is represented in the Bra-ket notation, in which the first number marks the number of photons in the cavity and the letter represents the state of the two level (g stands for the ground state and e stands for the excited state).

The coupling constant between a photon and the TLS is given by $g = \vec{E} \cdot \vec{d}/\hbar$, where $\vec{E}$ is the electric field of the photon and $\vec{d}$ is the dipole moment of the TLS. H_γ describe the loss of excitation of the TLS to other modes of the cavity, where γ is the decay rate. The coupling of the cavity described by H_κ, where κ is again the decay rate [5]. An interesting regime is, if γ and $\kappa < g$, strong coupled regime. The coupling constant g can be measured, if the cavity resonance frequency ω_r is equal to transition frequency Ω and if there is no damping. Then $|n+1, g\rangle$ and $|n, e\rangle$ are degenerated and the system oscillates with the frequency g/π between the symmetric and the asymmetric superposition state. The energy separation between the two states is $2\hbar\sqrt{n+1}g$ [6]. Therefore the resonance of the cavity is split and this allows to measure the coupling constant g.

2.2 Circuit QED

There are many systems, that realize the Jaynes-Cummings Hamiltonian. A new and promising one is circuit QED. In circuit QED the resonator is a coplanar waveguide for microwave photons (section 2.4.2), that couples to a TLS (artificial superconducting atom). Circuit QED is an one dimensional variant of cQED. The advantage of circuit QED over cQED is the strong coupling to the TLS, which depends on the mode volume in the cavity ($g \propto \frac{1}{\sqrt{V}}$). In a resonator (one dimensional microwave cavity) the mode volume is six magnitudes smaller than in a three dimensional cavity and thus the coupling is 1000 times larger. Fig. 2.1 shows a sketch of such a waveguide resonator and its interaction with two different TLS (artificial and Rydberg atoms). Since every part of this system can be describe as an electric circuit, the system is called circuit QED.

2.2.1 Microwave Resonator

The microwave resonator can be modeled as an oscillating circuit consisting of a capacitance C and an inductance L, which are connected in series. The current I and the charge Q of such a system show the well-known behavior of a classical harmonic oscillator with the resonance frequency $\omega = \frac{1}{\sqrt{LC}}$. The energy spectrum of such a system is $E = \hbar\omega(n + \frac{1}{2})$.

The waveguide resonator consists of two ground planes and a center conductor (Fig. 2.1). The TLS couples to the electric field between the center conductor and the ground planes. More theory on waveguide resonators can be found in section 2.4.

2.2.2 Superconducting Qubit

A quantum harmonic oscillator consists of a capacitance and an inductance. The current and the charge $\hat{I}$ and $\hat{Q}$ are operators with the commu-

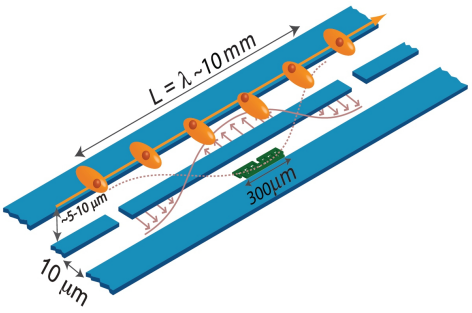

Figure 2.1: A schematic representation of a microwave transmission line resonator coupling to an atifitional atom (green box) and to Rydberg atoms (orange balls). The red arrows symbolize the electric field in the resonator. Since the length of the resonator is a factor of 10^3 longer than its width and height, the mode volume is six magnitudes smaller than in a three dimensional cavity and thus the coupling between the TLS and the photons is around 10^3 times larger

tation relation $[\hat{Q}, \hat{I}] = \hbar i$.

Thus all the eigenenergies are separated by $\hbar\omega$ like in the case of the waveguide resonator. Therefore such a system cannot be used as a qubit, since the photons in the cavity couple to all energy levels.

The quantum harmonic oscillator has a harmonic spectrum. A new component called Josephson junction makes the oscillator non-harmonic. A Josephson junction is made of two superconductors with a thin layer of insulator between them. A current can flow between the two superconductors by cooper pairs tunneling through the layer. If two Josephson junctions are connected in parallel, a current can flow either in one direction or in the other. This defines two states, that are degenerated and using the asymmetric state $|e\rangle$ and the symmetric state $|g\rangle$ can defined a TLS. The non-linearity of the two Josephson junction is thus transferred to the circuit, which becomes anharmonic and the system can be used as a superconducting qubit. Such an anharmonic oscillator is also called an artificial atom, because a) it has discrete, anharmonic energy levels like an atom and b) shows typical properties of an atom like the Stark and the Zeeman effect. This system can couple to a photon in the resonator like described in section 2.1. Unfortunately these artificial atoms lose their excitation within a few microseconds. This is unimportant for fast calculation, but for longer calculation we need an opportunity to save the information for a short moment, RAM. Therefore another long-living anharmonic system is needed. The combination of a short-living qubit used as processor and a long-living qubit used as RAM is called a hybrid system and is explained in the next section.

2.3 Hybrid System

An excited quantum mechanics state is not stable. It will decay as a consequence of the coupling to the vacuum fluctuation of the electromagnetic field of the environment. Therefore a qubit will lose its quantum information after a certain time, called the decoherence time of the system. If the system is weakly coupled to the surroundings (including the resonator), the decoherence time is long, but the time, an operation on the qubit takes, is longer as well. Therefore the number of operation on a qubit is limited by this time. A possible solution to this problem is to use a hybrid system. In a hybrid system two sorts of qubits with different coherence times are used for example in this experiment circuit QED and Rydberg atoms. Superconducting qubits have short coherence time, but couple strongly to the photons. Therefore we need a qubit with long coherence time: e.g. Rydberg atoms. The operation will be executed on the qubit with the shorter coherence time (superconducting qubit), which forms the processor of the quantum computer. The information will then transported by entanglement to the qubit with the longer coherence time (Rydberg atom) before it decays. Thus the Rydberg atoms form the RAM. The information is sent back to from the RAM to the Processor after it is reinitialize.

A superconducting circuit has a huge size compared to a Rydberg, therefore it couples stronger to the photons in the cavity, the coherence time is shorter and it can be used for fast operations. The superconducting circuit and the Rydberg atoms are both coupled to the cavity and can therefore be entangled. For this reason the information can be transported to the Rydberg atom, which is weaker coupled to the surroundings and has therefore a longer coherence time.

2.3.1 Rydberg Atom

A true alternative for quantum computation on a timescale of milliseconds instead of microsecond in the case of superconducting qubits are Rydberg atoms, since they live longer and couple strongly to microwave resonators. An Rydberg is a highly excited atom and thus consists of a positive charged nucleus and a weakly coupled electron on the outer shell. For example the simplest atom is the hydrogen atom, which consists only of a proton and an electron. The energy levels E_n can be calculated by solving the Schrodinger equation:

$$-\frac{\hbar^2}{2m}\nabla^2\psi(r,\vartheta,\varphi) - \frac{e^2}{4\pi\epsilon_0 r}\psi(r,\vartheta,\varphi) = E_n\psi(r,\vartheta,\varphi), \tag{2.2}$$

which leads to discrete values. These energies only depend on the principal quantum number n:

$$E_n = -\frac{Ry}{n^2}, \tag{2.3}$$

where Ry is the ground states energy. A hydrogen atom is a Rydberg atom, if the principal quantum number n is high .

In a nonhydrogenic atom the energy structure is different. There is still a core with positive charge and an electron, contrary to the hydrogen atom the core cannot be seen as pointlike but of a finite size. Depending on the angular momentum l, the electrons may penetrate into the core. The different potential in the core shifts the energy levels. The electron has a higher probability to penetrate the core at low l states. One finds, that the energy levels of every atom can be expressed as:

$$E = -\frac{Ry}{(n-\delta_l)^2}, \tag{2.4}$$

where δ_l is called the quantum defect. The quantum defect does hardly depend on the principal quantum number n and is only large for low l states. It is very hard to calculate quantum defects and they are found by experiments.

The coupling between a (Rydberg) atom and the electric field of a microwave photon depends on the electric dipole of the atom, which is defined as the charge of the electron and the proton times the distance between them $\vec{d} = e \cdot \vec{r}$. Since the distance between the core and the electron in a Rydberg atom is proportional to n^2, the electric dipole moment is proportional to n^2. Therefore the electrical dipole moment is strong in a Rydberg atom, for example $d \approx 1500\ D$ for a state with $n = 60$.

Due to the strong dipole on electric field drastically shifts the energy levels. The shifts can show a linear (quadratic) dependence on electric field strength E, this is then called the linear (quadratic) stark effect. There are both red (down) shifted and blue (up) shifted states with respect to the energy. Spherical coordinates are replaced by parabolic coordinates, that diagonalize the Hamiltonian for a small field. Thsi means, that quantum number l is replaced by n_1 and n_2. for hydrogen this leads to: [7]

$$n = n_1 + n_2 + |m| + 1 \qquad E_{n,n_1,n_2} = -\frac{Ry}{n^2} + \frac{3}{2}E(n_1 - n_2)n. \tag{2.5}$$

The dipole of the Rydberg atom is quantized by $k = n_1 - n_2$. The energies of the highest n and the lowest n+1 state cross around $E = \frac{1}{3}n^5$. In hydrogen the two states do not couple as a consequence of the conservation of the Runge-Lenz-vector and therefore the crossing of different states is not

avoided (Fig. 2.2 a)). For all others atoms the interaction with the core electron leads to violation of this conserved quantity and the crossings are avoided (Fig. 2.2 b)). [7]

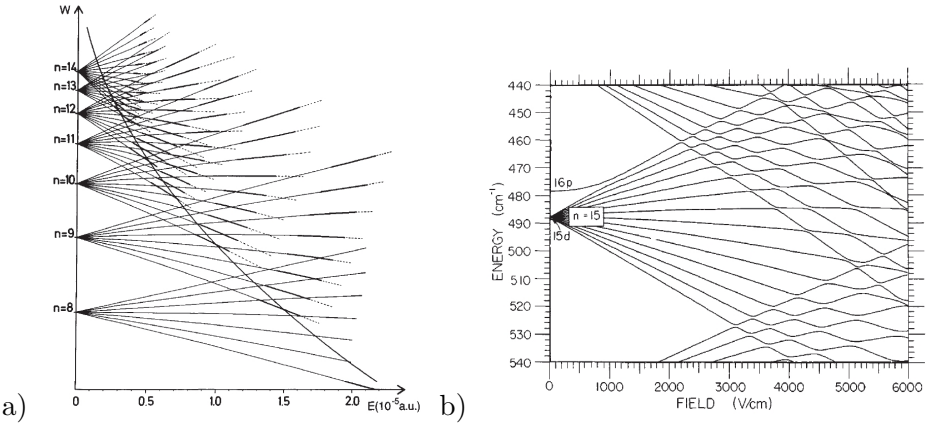

Figure 2.2: The energy of the states $|m| = 1$ as a function of the electric field of a) hydrogen (from [8]) and b) sodium (from [9]).

The difference between two energy levels of zero field gets smaller for high n. But with modern equipment it is possible to excite the state $|n\rangle$ to $|n+1\rangle$ by a microwave photon for high n (≈ 50). Therefore Rydberg atoms in cavity QED (for example in a coplanar waveguide resonator) can be used for quantum computation.

Fig. 2.3 shows the potential of a Rydberg atom with and without an external electric field. Pulsed electric field-ionization can be used to detect the state of a Rydberg atom by applying a high electric field $E \approx \frac{1V}{cm}$. The potential with the electric field has a saddle point. If an electric field is applied to Rydberg atoms, those of them, who has a quantum number n higher than the energy of the saddle point, will be ionized. Therefore by detecting the ions, the quantum number n of a Rydberg atom can be measured and can therefore be used as read-out of the qubit state.

The lifetime of a state of an atom is given by the Einstein coefficients $A_{n'l',nl}$, which is defined as;

$$\left(\frac{dN}{dt}\right)_{A_{n'l',nl}} = -A_{n'l',nl}N, \tag{2.6}$$

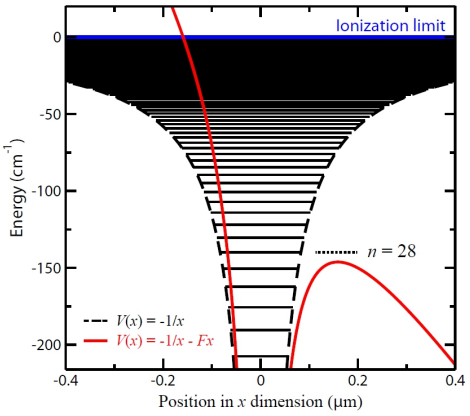

Figure 2.3: The potential of a Rydberg atom without (black) and with (red) electric field. The blue line shows the ionization energy without an electric field. Applying an external electric field tilts the potential (red) and a new ionization field at the saddle point forms. Here, $n = 28$ corresponds to the first state, that is ionized by the field.

where $n‘, l‘$ labels the higher and n, l labels the lower state and N describes the population. In the case of a Rydberg atom $A_{n‘l‘,nl}$ is given by: [7]

$$A_{n‘l‘,nl} = \frac{4e^2\omega^3_{n‘l‘,nl}}{3\hbar c^3}\frac{l_{max}}{2l+1}\left|\langle n‘l‘|r|nl\rangle\right|, \tag{2.7}$$

where l_{max} is equal to maximum value of l and $l‘$. The dipole transition is only allowed if $n‘ = n \pm 1$ and $l‘ - l = -1, 0, 1$. Therefore the lifetime depends strongly on l. The lifetime of a state with low l scales with n^3. For the state with l=n-1 the lifetime scales with n^5. The coherence time of a state with high l at $n \approx 50$ is range of micro second and an order of magnitude higher than the coherence time of a superconducting qubit, whose coherence time is around nano second. Therefore Rydberg atoms are good candidates for quantum RAM, since they live long enough, couple good to microwave photons and have anharmonic energy levels. You can make a huge number of operation on the superconducting qubit (processor) until the information in the Rydberg atoms (RAM) is vanish.

2.4 Coplanar Waveguide

2.4.1 The general Design of a Waveguide

In free space electromagnetic waves propagate in all directions and with the speed of light, which is

$$c = \frac{1}{\sqrt{\mu_0 \cdot \epsilon_0}} = 299792458\ m/s \tag{2.8}$$

for vaccum. An important quantity for reflexion and transmission of a electromagnetic wave at a boundary layer is the impedance, which is defined as

$$Z = \frac{E}{H} = \sqrt{\frac{1}{\mu_0 \epsilon_0}} \tag{2.9}$$

where E is the electric and H the magnetic field. In vacuum the impedance Z is equal to 377 Ω [10]. In a material ϵ_0 changes to $\epsilon_0 \cdot \epsilon_r$, where ϵ_r is called the dielectric constant and is a dimensionless quantity, which depends on the material.

A waveguide is a structure, which conveys electromagnetic waves between its endpoints. To analyze the electric and magnetic field in the waveguide Maxwell's equations are used with boundary conditions defined by the materials and the geometry of the waveguide. [11]
The waveguide has an effective dielectric constant ϵ_{eff}, which is not equal to the dielectric constants of the materials ϵ_r, but depends also on the geometry of the waveguide. The effective dielectric constant can be calculated by conformal mapping and it holds:

$$\epsilon_{eff} = \frac{1 + \epsilon_r \cdot K_K}{1 + K_K}, \tag{2.10}$$

where

$$K_K = \frac{K(k`) \cdot K(k_2)}{K(k) \cdot K(k_2`)}, \tag{2.11}$$

$$k_2 = \frac{tanh(\pi \cdot S/4 \cdot h)}{tanh(\pi \cdot (S + 2W)/4 \cdot h)} \tag{2.12}$$

and

$$K_2` = \sqrt{1 - k_2^2}. \tag{2.13}$$

This leads also to an effective impedance (Eq. 2.9) and to an effective speed of light (Eq. 2.8) in the waveguide, which is not equal to the vacuum speed of light. A common standard for a waveguide is an impedance of 50 Ω. There are different designs of waveguides. The one used in this thesis is a coplanar waveguide.

A coplanar waveguide is patterned onto a metallic coating on a dielectric substrate. The metal is etched away at two parallel running lines of width S forming the metallic center conductor, which is not connected to the metallic ground planes. Fig. 2.4 shows a sketch of such a coplanar waveguide, where t is the thickness of the metal, s marks the gap distance between the center conductor and the ground planes and w is the thickness of the center conductor.

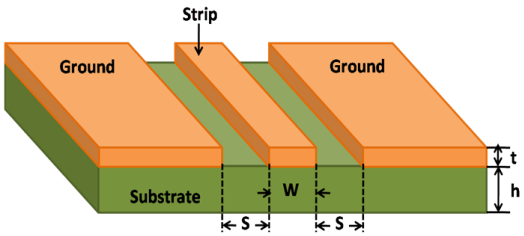

Figure 2.4: Schematic representation of a coplanar waveguide. From [12]

2.4.2 Resonator in a Coplanar Waveguide

If the center conductor of a coplanar waveguide is broken at two points on the waveguide, there are two impedance mismatches like a Fabry-Perot cavity in optics. The coplanar waveguide between the broken center conductor forms a resonator. Fig. 2.5 shows such a broken center conductor. The microwave forms a standing wave between this two points and there are a set of discret modes.

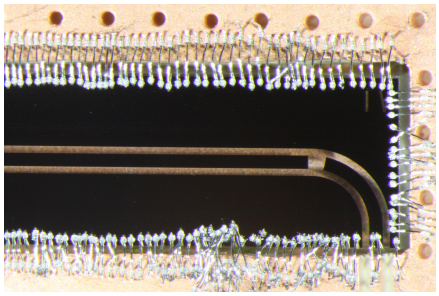

Figure 2.5: Picture of a resonator. The black part is metallic. The two bright strips are the dielectric material. The center conductor has one gap, which leads to an impedance mismatch in the waveguide.

A coplanar transmission line resonator can be mapped into an electrical circuit (Fig. 2.6 a)). The resistance of the coplanar waveguide R_L is typically 50 Ω. The gaps in the center conductor are represented by a capacitance C_κ. R_l, C_l and L_l are the resistivity, the capacity and the inductance per unit length of the transmission line and l is the length of the resonator. This circuit is equivalent to the circuit in Fig. 2.6 b) with different parameter. It holds: [13]

$$L_n = \frac{2L_l l}{n^2\pi^2} \tag{2.14}$$

$$C = \frac{C_l l}{2} \tag{2.15}$$

$$R = \frac{Z}{\alpha l} \tag{2.16}$$

$$R^* = \frac{1 + \omega_n^2 C_\kappa^2 R_L^2}{\omega_n^2 C_\kappa^2 R_L} \tag{2.17}$$

$$C^* = \frac{C_\kappa}{1 + \omega_n^2 C_\kappa^2 R_L^2}, \tag{2.18}$$

where α is attenuation constant of the resonator, $\omega_n = \frac{1}{\sqrt{L_n C}}$ is the angular frequency of the resonator and n marks the number of the resonance mode. For small capacity C_κ and small angular frequency the capacitor C^* is equal to C_κ.

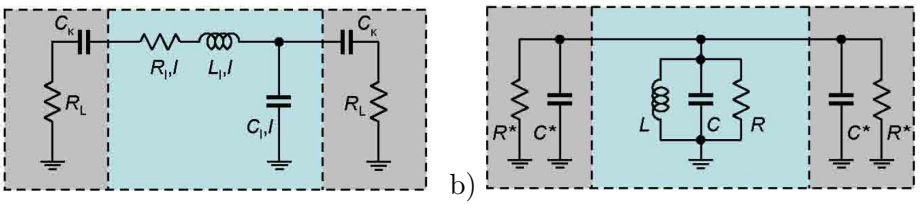

Figure 2.6: Schematic representation of a coplanar waveguide resonator. The circuit in a) and b) have the same properties. Eq. 2.14 to 2.18 connect the two representation. [13]

2.4.3 Transmission Spectrum of a Resonator

A perfect isolated and lossless resonator ($C_\kappa \to \infty$, $R_l \to 0$) only allows microwaves with discrete frequencies to be transmitted through the resonator. These frequencies are:

$$f_n = n \cdot \frac{c}{2\sqrt{\epsilon_{eff}} \cdot l} = \frac{1}{2\pi\sqrt{L_n C}}, \tag{2.19}$$

where n is a natural number and marks the number of the mode. At finite coupling and resistance the resonances of the transmission spectrum are of Lorentzian shaped:

$$S(f) = A_0 \cdot \frac{\delta f}{\delta f^2/4 + (f - f_0)^2}. \tag{2.20}$$

The frequency f_0 is the resonance frequency and δf is the full width half maximum (FWHM) of the resonator. Fig. 2.7 shows an example of aLorentzian function in logarithmic scale. The FWHM is taken at 3.1 dB (logarithmic scale) under the maximum.

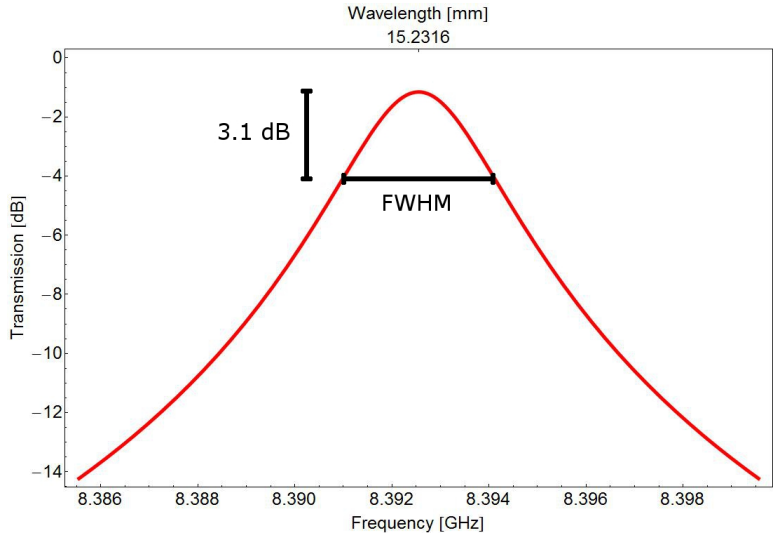

Figure 2.7: The transmission spectrum of a resonator. The spectrum forms a Lorentzian function (Eq. 2.20). The FWHM δf lies in logarithmic scale 3.1 dB under the maximum, what is the half in linear scale.

The quality factor of a resonance is defined as

$$Q = \frac{f_0}{\delta f}. \tag{2.21}$$

For a perfect and lossless resonator the Q-factor is infinite. The quality factor depends on the external coupling of the resonator and its internal losses, where each Q-factor can be assigned to. The external and the internal quality factor and the coupling coefficient are defined as:

$$Q_{ext} = \frac{\omega_n R^* C}{2} \tag{2.22}$$

$$Q_{int} = \omega_n RC = \frac{n\pi}{2\alpha l} \tag{2.23}$$

$$g = \frac{Q_{int}}{Q_{ext}}, \tag{2.24}$$

where $\omega_n = 2\pi \cdot f_n$. A resonator with $g > 1$ is called overcoupled, with $g < 1$ undercoupled and $g = 1$ defines critical coupling. The connection between the internal and external to the total measured Q-factor is given by: [13]

$$\frac{1}{Q} = \frac{1}{Q_{ext}} + \frac{1}{Q_{int}}. \tag{2.25}$$

The insertion loss is defined as

$$L_0 = -20 \cdot log(\frac{g}{g+1}) \tag{2.26}$$

and is given in dezibel. A finite C_κ shifts also the resonance frequency:

$$f_n^* = \frac{1}{2\pi \cdot \sqrt{L_n \cdot (C + 2C^*)}} \tag{2.27}$$

The transmissions spectrum of a coplanar waveguide with a resonator can be calculated by the ABCD-matrix analysis. Each element (transmission line, capacitors) has a specific matrix and the transmission ABCD-matrix of the system is equal to the product of the input, transmission and output matrix. It holds: [13]

$$\begin{pmatrix} A & B \\ C & D \end{pmatrix} = \begin{pmatrix} 1 & Z_{in} \\ 0 & 1 \end{pmatrix} \cdot \begin{pmatrix} t_{11} & t_{12} \\ t_{21} & t_{22} \end{pmatrix} \cdot \begin{pmatrix} 1 & Z_{out} \\ 0 & 1 \end{pmatrix}, \tag{2.28}$$

where

$$\begin{aligned} t_{11} &= cosh(\gamma l) \\ t_{12} &= Z_0 sinh(\gamma l) \\ t_{21} &= 1/Z_0 sinh(\gamma l) \\ t_{22} &= cosh(\gamma l), \end{aligned}$$

with input/output impedances $Z_{out/in} = 1/i\omega C_\kappa$ and with the transmission line propagation coefficient $\gamma = \alpha + i \cdot \beta$. This matrix can then be converted to the S-parameters (section 3.4). For more information see [13].

2.4.4 Superconducting Waveguide

Superconducting Materials

The conductivity in a normal metal is increasing, when temperature is decreased. Superconductors undergo a phase transition and lose any resistivity under a certain temperature T_c. There is just a thin layer on the surface, typical on the order of 100 nm, where the magnetic field is finite. The magnetic field decreases exponentialy in the bulk of the characteristic length of the London penetration depth λ. The current in the superconducting material is transported by so called cooper pairs, a coupled pair of two electrons in the lattice. [14]

Transmission Line Inductance

Eq. 2.14 gives the inductance of the resonator as a function of the inductance per unit length. The induction per unit length is given by: [15]

$$L_l = L_l^m + L_l^k, \tag{2.29}$$

where L_l^m is the magnetic inductance resulting from the geometry of the transmission line. In a coplanar waveguide the magnetic induction is given by: [15]

$$L_l^m = \frac{\mu_0}{4}\frac{K(k')}{K(k)}, \tag{2.30}$$

where K(k) is the complete elliptic integral of the first kind. L_l^k is called the kinetic inductance and appears only in superconducting system. It results from the inertia of the cooper pairs. The kinetic inductance is important in superconducting waveguids, because it shifts the resonance frequencies down. This effect can be very strong in thin waveguides and at temperature near to the critical temperature (section 4.3). For the kinetic inductance holds: [15]

$$L_l^k = \mu_0 \frac{\lambda^2}{t \cdot w} g(s, w, t) \tag{2.31}$$

The factor $g(s, w, t)$ depends only on the geometry of the coplanar waveguide and it holds:

$$g(s, w, t) = \frac{1}{2}k^{-2} \cdot K^{-2}(k) \cdot \left\{ -Log\left(\frac{t}{4w}\right) - k \cdot Log\left(\frac{t}{4d}\right) + 2\frac{d'}{d} Log\left(\frac{s}{d'}\right) \right\}, \tag{2.32}$$

where $d = w + 2s$, $d' = w + s$, t is the thickness of the metal, w is the width of the center conductor and S is its distance to the ground plane (Fig. 2.4). The London penetration depth λ depends on the temperature, the critical temperature of the material and the resistivity in the normal state at T_c: [15]

$$\lambda = \lambda(0) \cdot \theta_\lambda, \tag{2.33}$$

where

$$\theta_\lambda \approx \frac{1}{\sqrt{1 - (\frac{T}{Tc})^4}} \tag{2.34}$$

is the temperature dependent part and

$$\lambda(0) = \sqrt{\frac{\rho(T_c)}{T_c}} \cdot 1.05 \cdot 10^{-3} m \tag{2.35}$$

is the London penetration depth at zero temperature.

Fig. 2.8 shows the temperature depended of the kinetic inductance divided by the magnetic induction for NbTiN as a function of the temperature.

For more information see [15]. The kinetic inductance leads to a decrease of the resonance frequency (Eq. 2.14 and 2.29), which cannot be neglect in a NbTiN chip.

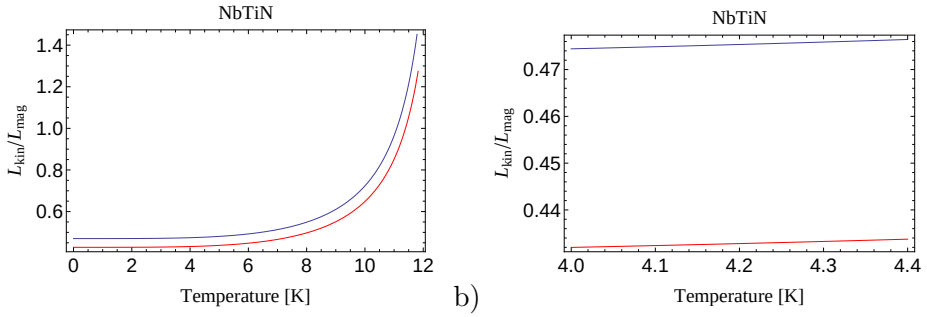

a) b)

Figure 2.8: Two plots of the temperature dependence of the kinetic inductance divided by magnetic induction for NbTiN ($T_c = 13.1\ K$) for the geometry of sample G2B1 ($w = 160\ \mu m$, $s = 80\ \mu m$, $d = 150\ nm$ and $\rho(T_c) = 67 \cdot 10^{-8}\ \Omega \cdot m$) in blue and for the geometry of sample B0RG1 ($w = 160\ \mu m$, $s = 80\ \mu m$, $d = 150\ nm$ and $\rho(T_c) = 67 \cdot 10^{-8}\ \Omega \cdot m$) in red a) from zero kelvin to the critical temperature and b) near to the boiling point of Helium (4,2 K). The values of G2B1 are scaled by a factor of 10

Chapter 3

Measurement Setup

In this chapter the measurement setup with its different components are introduced. The most interesting part of the experiment is the superconducting chip. Its structure and fabrication are discussed in section 3.1. The chip is glued to a PCB (Printed Circuit Board), which connects the coplanar waveguide of the chip with the coaxial cables running to the VNA (section 3.2). The PCB is screwed to a dipstick, which allows to dip the PCB with the chip in a liquid helium dewar, what decrease the temperature of the chip to 4.2 K (section 3.3). Finally the operating mode of the VNA is explained in section 3.4.

3.1 Superconducting Chips

3.1.1 NbTiN

The goal of the experiment is to couple Rydberg atoms to a coplanar waveguide and use those coupled atoms as a RAM for a quantum computer (see section 2.3). The resonance frequencies for the interesting states of the Rydberg atoms lie in a range of 27 GHz. Therefore it is necessary to design resonators with this frequency range. Since the Rydberg atoms are used as a RAM, the time, in which they interact with the microwave photons, should be long enough. Thus the resonator length should be in the range of centimeters and therefore higher harmonic resonances are needed. For example, the third harmonic mode is needed to reach frequencies around 27 GHz for a resonator with a length of 7 mm. Also a high Q-factor is wanted, in order to distinguish the two states of strongly coupled Rydberg atom. Since the Q-factor is decreasing as a function of the mode number (Fig. 4.17), a waveguide with a high Q-factor at the fist mode is required. The Q-factor also depends on the critical temperature T_c of the superconductor of the waveguide. In previous experiments Niobium (Nb) was used, which has a critical temperature $T_c = 9.2\ K$ [16]. In these experiments a new alloy called Niobium Titanium Nitride (NbTiN) with a critical temper-

Sapphire

h	ϵ_r	Loss tangent $tan(\delta)$
508 μm	10.7	$1 \cdot 10^{-4}$ [17]

NbTiN

t	T_c	$\rho(T_c)$	$\mu(0)$
150 nm	13.1 K	$6.7 \cdot 10^{-7} \Omega m$	$2.23861 \cdot 10^{-7}$ m

Design of the chips

S	ϵ_{eff}	L_l^m
160 μm	5.9	$4.13667 \cdot 10^{-7}$ H
W	Z_0	C_l
80 μm	49.3 Ω	$1.59796 \cdot 10^{-10}$ F

Table 3.1: Properties of the NbTiN transmission lines on sapphire used in these experiments. The Loss tangent $tan(\delta)$ is the angle in a complex plane between the resistive (lossy) and its reactive (lossless) component of an electromagnetic field [18]. W is the width of the center conductor and S is the distance between the center conductor and the ground plane.

ature $T_c = 13.1\ K$ is examined and its microwave properties are determined. The dielectric material is sapphire ($\alpha - Al_2O_3$) with a dielectric constant ϵ_r of 10.7. Tab. 3.1 shows an overview of the properties of a NiTiN/sapphire coplanar waveguide used in this experiment.

3.1.2 Fabrication of the Chip

The samples used in this experiment are made by the technique of photolithography. First the metal (NbTiN) is sputtered on to the dielectric (sapphire). Then a positive photoresist (AZ-1506) is spinned onto the metal, which is not stable against UV-light. Then, the sample is covered with a mask, that is transparent, where the metal should be etched away and then is exposed to UV-light. At the exposed positions the photoresist changes its chemical properties and is soluble in methyl isobutyl ketone (MIBK) and isopropanol. The sample is now exposed to a chemically reactive plasma (Ar-SF6). The parts under the photoresist are protect and just the uncovered metal is etched away. Fig. 3.1 shows a schematic representation of the whole operation sequence. For a closer look, see [19]. [20]

At the end the photoresist is removed by aceton and isopropanol. Therefore the chip is washed in isopropanol for 10 min at 50° C with ultrasound. Then the chip is washed with aceton for 10 min at 50° C with ultrasound and again with isopropanol for 5 min at 50° C with ultrasound. Finally the chip is blown off by N_2.

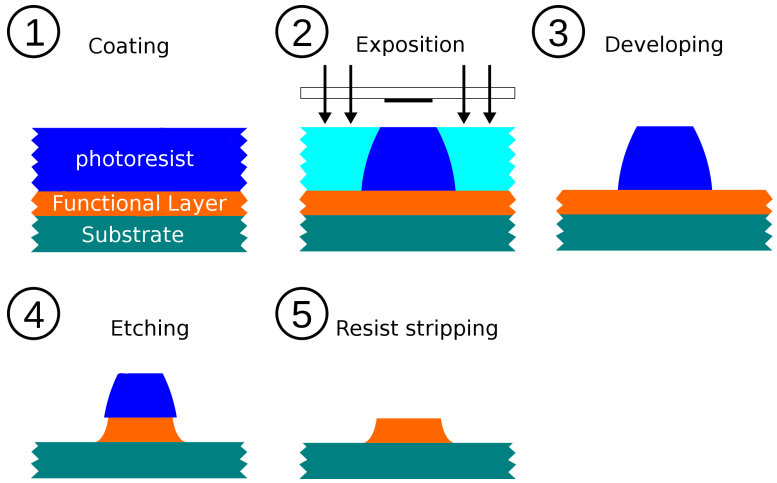

Figure 3.1: Operating sequence of a photolitohography. The green part symbolize the dielectric material (sapphire), the orange part is the superconducting metal (NbTiN) and the blue part is the photoresist. The first picture shows the sample before, picture 2 during and picture 3 after exposing the sample to UV-light. Picture 4 shows the sample after the plasma etching and picture 5 after the photoresist is soluble. [19]

3.1.3 Connection to the VNA

To determine the microwave properties of the transmission spectrum of the superconducting waveguide, it is necessary to connect the chip to a vector network analyzer (VNA). This device sends microwaves through the chip and measures the S-matrix of the chip (see section 3.4). The small chip is thus glued into a Printed Circuit Board (PCB) , that allows the transmission line of the chip to be connected to a MMPX-connector (section 3.2). The PCB is than screwed into a dipstick and is connected to the VNA by long copper coaxial cables (section 3.3).

3.2 PCB

The PCB (Printed Circuit Board) consists of Polytetrafluoroethylene (PTFE) as a dielectric material. The dielectric is 508 μm thick and is covered with a 35 μm thick layer of copper (Cu). The PCB contains of two transmission lines, that on one end are connected to coaxial print MMPX-connectors, that are soldered on to the PCB. These adapters connect the coplanar waveguide of the PCB with the coaxial cables connected to the VNA.

The other end of the transmission lines end in a gap in the middle of the PCB, where superconducting chip will be glued into (Fig. 3.2). Aluminum

a) 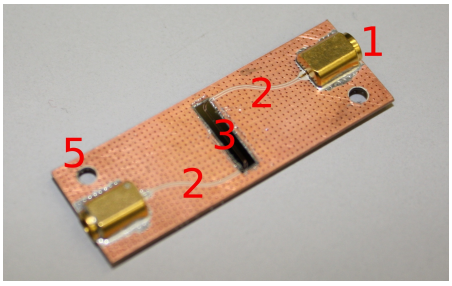

b) 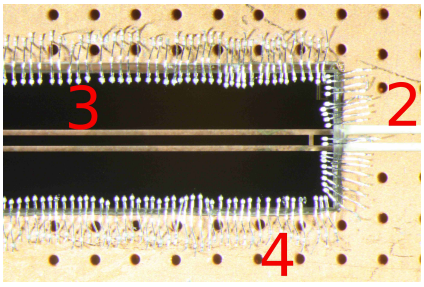

Figure 3.2: A PCB with a chip in the center. a) is the full sight and b) is a zoom into it. The print MMPX-connectors (1) are connected over the transmission lines of the PCB (2) to the chip (3) in the center of the PCB by aluminum bonds (4). The hole (5) is to screw the PCB on the sample holder in the dipstick

Power (1)	Time (1)	Force (1)	Loop height	Wire tail
200 mW	90 ms	Low	66 (= 1676 μm)	56 (= 314 μm)

Power (2)	Time (2)	Force (2)	Wire pull	Dual force
215 mW	90 ms	High	33 (= 185 μm)	On

Table 3.2: Setting of the manual wire bonder in these experiments. (1) marks the first contact of the bond (to the PCB) and (2) marks the second contact of the bond (to the chip). The meaning of the parameter are describe in [21].

bonds connect the ground plane of the PCB with the ground plane of the chip and the central conductor of the chip with the central conductor of the PCB. In this waveguides of the PCB and of the chip are properly connected and the microwaves can pass through the whole sample. The bonds have a diameter of 25 μm and are soldered by a manual wire bonder. The wire bonder does not solder the aluminum wires by heating the wires, but solders by applying pressure and treating the wires with ultrasound to the surface [21]. A positive side effect of the bonds is, that the sample is supporting the glue holding the chip in the PCB. The settings of the manual wire bonder in these experiments can be seen in Tab. 3.2.

Fig. 3.2 shows two pictures of a sample consisting of a PCB and a chip in the middle. Picture a) shows the hole PCB with the coaxial print MMPX-connectors on both sides. Picture b) shows a zoom to the chip and shows the aluminum bond wires, which connect the chip and the PCB.

3.3 Dipstick and Dewar

3.3.1 Dipstick

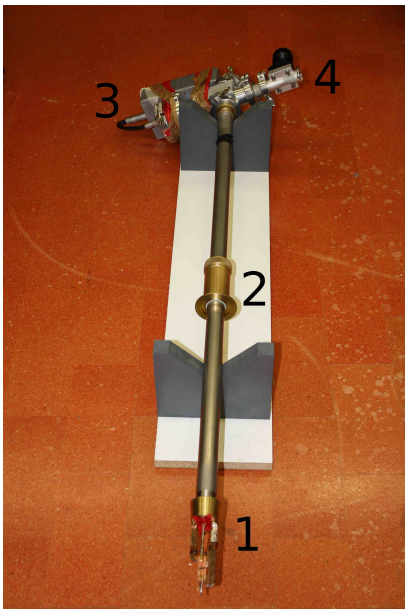

Figure 3.3: Picture of the dipstick. The Sample holder (1) holds the PCB. The abrasive sleeve (2) on the dipstick is free to move and connects the dipstick with the top flange of the helium dewar. On top of the dipstick are the connector plugs for the coaxial cables, the temperature sensor and the heating wire cables (3) and a valve for the pump (4).

Since NbTiN has a critical temperature of 13.1 K, the sample has to be cooled down to at least this temperature. The easiest way to do this, is to dip the sample in liquid helium, which has a boiling point of 4.2 K at normal pressure. The sample is thus attached to a so called dipstick, which is used to dip the sample in a dewar filled with liquid helium. Fig. 3.3 shows a picture of the dipstick used in this thesis and Fig. 3.5 shows a dipstick in a dewar. The sample is screwed to the sample holder on the bottom of the dipstick. The dipstick is hollow in the middle and there are two coaxial waveguides, that run from the top of the dipstick to the PCB. The sample holder can be covered with a can, that can be evacuated (section 3.3.3)

Fig. 3.4 shows a zoom to the sample holder from the front and back. The two coaxial cables are connected to the coaxial print MMPX connectors of the PCB. Since they are made of copper, they are thermaly conducting and would heat the PCB. To avoid this, there are copper filaments from the

a) 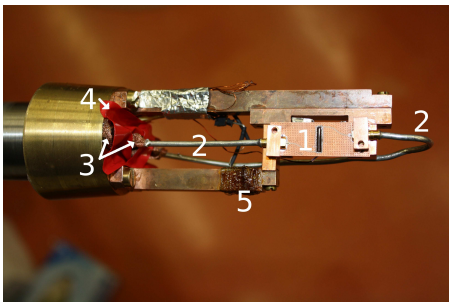

b) 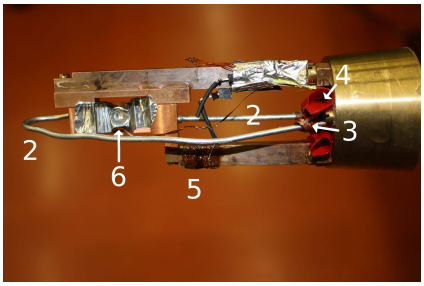

Figure 3.4: Zoom to the sample holder from the front a) and back b). The PCB (1) is connected to the two coaxial cables (2), which are thermally connected to the dipstick by copper filaments (3). The red tape (4) acts as a heat shield, that protects the sample from thermal 300 K radiation from the upper part of the dipstick. The temperature of the sample can be controlled by the heating wire (5) and is measured by the temperature sensor (6).

bottom of the dipstick soldered to the cables, which thermalize them with their cold environment.

3.3.2 Dewar

The dipstick is dipped into a dewar, that can be seen in Fig. 3.5. A dewar is a double-walled tank with a vacuum in between, which is a good thermal isolator. The dewar is filled with liquid helium (He^4) at normal pressure. The temperature of the helium will always stay at its boiling point of 4.2 K as long as the pressure is constant. The evaporated helium flows out over a pipe on the side of the dewar and will be recycled. On top of the dewar there is an Kf-40 flange for the dipstick. The abrasive sleeve on the dipstick, which is free to move, is fixed on the flange and so the dipstick can be lowered slowly into the liquid helium.

Most of the experiments are made at 4.2 K. For this temperature the setup described in this subsection suffices. For the temperature dependent measurements new components are needed, which are described in the next subsections.

3.3.3 Temperature Dependent Measurements

The kinetic inductance has an influence on the transmission spectrum of a superconducting coplanar waveguide resonator. For example the resonance frequencies are shifted and Q-factors are increasing. In contrast to the magnetic induction, the kinetic inductance is strongly temperature dependent

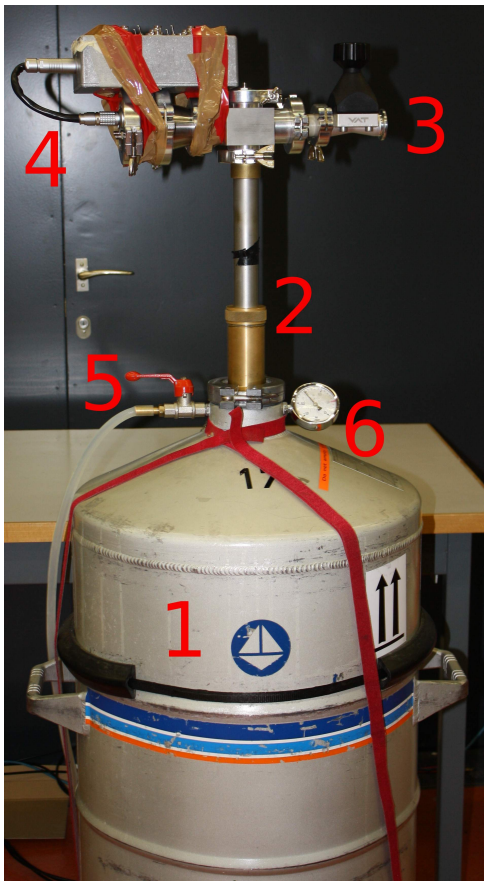

Figure 3.5: The helium dewar (1) with the dipstick connected by the abrasive sleeve (2). On top of the dipstick is a valve (3) for the pump and the connector plugs (4). The evaporated helium will run through the tube (5) and will be recycled. The pressure in the dewar can be measured by the barometer (6).

(see Eq. 2.34). Therefore it is interesting to measure the transmission spectrum at temperatures between 4.2 K and 13.1 K. As long as the sample has a direct contact with liquid helium, it is not possible to heat it. So a setup, which allow us to shield the sample from the helium and to manipulate and to measure the temperature of the sample, is needed.

Vacuum Pump and the Cylinder

The sample holder needs to be protected from direct contact to liquid helium. Therefore a metallic cylinder is put over the bottom of the dipstick. A picture of the cylinder over the sample holder can be seen in Fig. 3.6. The inside of the dipstick will be evacuated by a vacuum pump to a pressure in the range of 10^{-5} $mbar$. In order to close the cylinder airtight, vacuum grease is deposited on the boundary surface between the dipstick and the cylinder. On the one hand evacuating the dipstick attached the cylinder at the dipstick without any clamps. On the other hand the vacuum in the cylinder avoids thermal convection between the inner wall of the cylinder and the sample. Thus the main cooling of the sample is achieved over the two copper rods of the sample holder.

The sample holder is now thermally isolated enough, that can be heated without wasting too much helium. Therefore a manganin heating wire is used, which is explained in the next subsection.

Figure 3.6: The sample holder covered by a metallic cylinder. The cylinder protects the sample from direct contact to the helium and thus allows so to heat the sample to the desired temperature

Heating Wire

The dipstick with the cylinder over the dipstick will dipped in the helium dewar like before without the cylinder. The temperature of the sample holder converges slowly to a certain temperature. The equilibrium temperature is higher than the boiling point of liquid helium, because the sample holder is heated by the upper part of the dipstick despite the thermal shields and the conducting filaments.

On the sample holder there is a heating wire wrapped around. A Picture of the wrapped wire can be seen in Fig. 3.4 The heating wire consists of manganin ($Cu_{84}Ni_4Mn_{12}$) and has a resistance of 94.7 Ω. The wire is connected by two wires made of copper running through the dipstick. The copper wires has a resistance of 2 Ω and can be neglect compared to the resistance of the heating wire. On top of the dipstick the two wires are connected to a power source. The current flowing through the heating wire will heat the sample holder. The wire is covered with GE Varnish, so it has a better thermal conductivity to the sample holder. There is a new equilibrium between the heating of the wire and the colling from the liquid helium. This temperature has been measured for different voltages and is showed in Fig. 3.7.

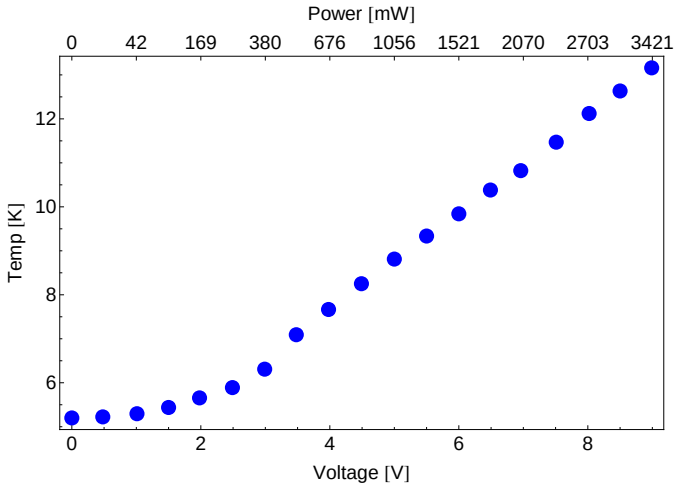

Figure 3.7: The equilibrium temperature of the sample for different voltages and powers of the heating wire. The curve looks linear as a function of the power in the interesting range

Temperature Sensor

A diode is an electric components consisting of a semiconductor with two different doping properties. At one side the semiconductor is doped with positive and on the other side with negative impurities. The resistance of the diode depends strongly on its temperature. Therefore such a diode can be used to measure the temperature in the cylinder. We use a Silicon Diodes DT-670 CU produced by LakeShore, which can be seen in Fig. 3.8. Fig. 3.4 shows the exact position of the diode on the sample holder. It is bonded on the back side of the PCB and so it measures direct the temperature of the superconducting chip.

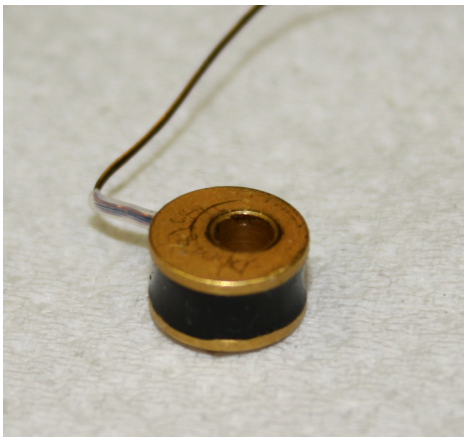

Figure 3.8: Picture of the Silicon Diodes DT-670 CU produced by LakeShore, which is used as temperature sensor in this experiment. The exact position of the diode on the dipstick can be seen in Fig. 3.4. [22]

The resistance of the diode is measured by the technique of four-terminal sensing. A schematic representation of the setup can be seen in Fig. 3.9 The diode has four contacts, two for the current and two for the voltage measurement. A voltage is applied between two of them and so a current is flowing through the diode. This leads to a voltage drop over the diode, which is measured by the other two contacts. The advances of a four-terminal sensing over a normal resistance measurement is, that the influence of the wire and contact resistances is eliminated by the separation of current and voltage. [23]

The four wires of the silicon diode are connected to a Cryogenic Temperature Controller (Model 325) produced by LakeShore. The temperature controller sends the current through the diode, measures the voltage drop over the diode and converts the resistance to temperature. Before the conversion works well, the temperature controller need to be calibrated. The temperature sensor is cooled down to three well-known temperature. We choose the boiling point of helium (4.22 K), the boiling point of nitrogen (77.36 K) and the freezing point of water (273.15 K) at normal pressure. The temperature controller measures the resistance at those temperatures and calculates the temperature curve as a function of the resistance. This procedure is called a SoftCal calibration and for more details see [24]. The accuracy of a 3-point SoftCal calibration in the interesting range of 2 K to 30 K is ± 0.5 K. [24]

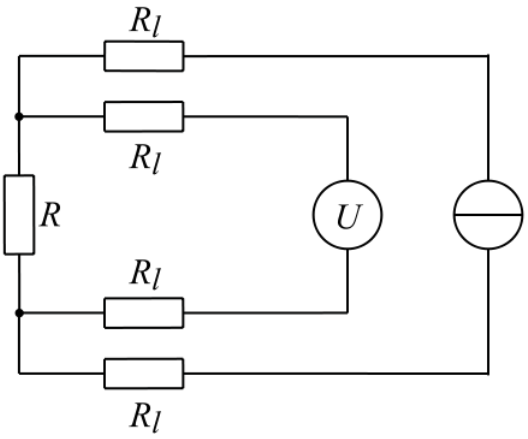

Figure 3.9: The schematic representation of a four-terminal sensing measurement of the resistance R of a silicon diode. The voltage measurement and the current are separated, what eliminates the influence of the wires and contact resistances R_l. [23]

3.4 Network Analyzer

The coaxial cables in the dipstick are connected to a two port VNA (ZVK Vector Network Analyzers produce by Rhode und Schwartz). The analyzer sends microwaves alternating through one port and measures the amplitude and phase of the reflected wave on the same port and the transmitted wave on the other port. Therefore there are four different spectrums: S_{11}, S_{12}, S_{21} and S_{22}, where the first number label the sending port and the second number the measuring port.

The analyzer has a range of 10 MHz to 40 GHz. It can do 1600 sweeps with a minimal bandwidth of 10 Hz and the dynamic range is higher than 110 dB. Most of the experiments were made with a power of -8 dBm (0 dBm are equal to 1 mW). In this range the accuracy of the amplitude is 0.2 dBm [25]. The S-matrix is averaged over a certain number of measurements, the average factor.

The coaxial cables has also loss and reflexion. It is necessary to eliminate this influence of the cables to the measurement of the transmission and reflexion of the resonators. This is done by a TOSM-calibration (Trough, Open, Short and Match). For this calibration four components are connected to the coaxial cables. The components and their properties can be seen in Tab. 3.3. Though is the only 2-port component and is connected to both cables at once. It shorts the two coaxial cables. The other components have just one port and are measured one after another. They connect the

	T	O	S	M
Number of Ports	2	1	1	1
Resistance [Ω]	-	∞	0	50
Reflexion	low	high	high	low
Transmission	high	-	-	-

Table 3.3: The properties of the four calibration components. The third row shows the resistances between the inner and outer conductor in the coaxial cable. The expected amplitude of the reflexion and transmission are given in the fourth and fifth row

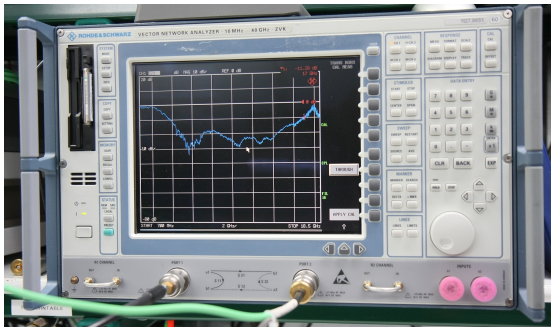

Figure 3.10: Picture of ZVK Vector Network Analyzers produce by Rhode und Schwartz from 10 MHz to 40 GHz. [26]

outer and inner conductor by a certain resistance (see Tab. 3.3) and end the coaxial cable. The analyzer measures the reflexion (at Trough also the transmission) for both cables and all components and calculates automatically the calibration parameters.

Chapter 4

Measurements and Results

The goal of the experiment is to couple Rydberg atoms to microwave photons and to use the long living states as RAM for long calculations (section 2.3). Since we use a new material, NbTiN, we need to characterize the microwave spectrum waveguide. This is done in five steps. At first the spectrum of the PCBs without a superconducting chip needs to be understood.

The center conductor of the PCB should have a width of $W \approx 140\ \mu m$ and have thus an impedance Z_0 of 50 Ω (section 2.9) and so matches with the impedance of the coaxial cables. A first series of PCB (Type 1) was badly made and have a center conductor with a width S of 73 μm (Fig. 4.1 a). A second series of PCB (Type 2) was better made and have a center conductor with a width S of 113 μm. The Type 2 PCB is expected to match better to the coaxial cables than Typ 1 PCB. It is also tested, if the results are reproducible. This means the S-matrix of two identical PCB are measured and the results are compared to each other (section 4.1). Secondly small NbTiN chips are glued in the PCB. These chips have a size of 2 $mm \cdot 9.3\ mm$ and the coplanar waveguide runs straight over the chip (section 4.2.1). The next step is to use bigger chips (4.3 $mm \cdot 9.3\ mm$), where the waveguides have curves and so the waveguides are longer. Therefore more higher harmonic resonances can be seen (section 4.2.2). In the end helium atoms will fly crossways over the PCB and therefore the waveguide over the chip has to be a long straight line. For this reason the chip is also crossways inserted to the PCB and the waveguide has to curve over the chip (section 4.2.3). Finally we measure the kinetic inductance of NbTiN and compare it for different geometries and temperatures (section 4.3).

4.1 PCB Tests

In these measurements we are only interested in PCBs contain only a transmission line. The waveguide directly connects one print connector to the other. Here we compare two PCBs: The Type 1 PCBs were manufac-

a) 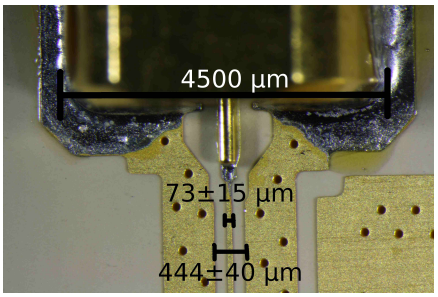

b) 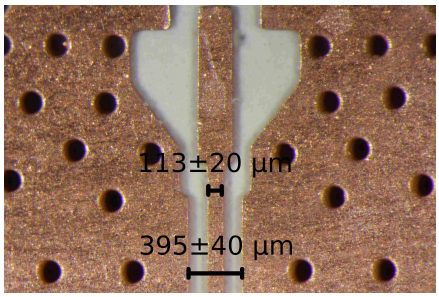

Figure 4.1: Pictures of a) a Type 1 PCB (with print connectors) and b) a Type 2 PCB (without print connectors) like it is used in this experiment. It can be seen, that the center conductor of the Type 2 PCB is wider than the center conductor of the PCB used in previous experiments. Type 1 PCB has a different colour, due to gold/silver layer on the top of the copper

tured with the Swiss company Optiprint and the Typ 2 PCBs with Hughes Inc. from USA. A zoomed picture onto the transmission line at the connector of this two PCB can be seen in Fig. 4.1, in which a) shows a Type 1 PCB and b) shows a Type 2 PCB we use in these experiments. We are interested in comparing the microwave spectrum of these two PCBs and the reproducibility among the Type 1 PCBs. Simulation are made using a program called microwave office, that simulates the transmission and the reflection between the two print connectors (section 3.4).

Since we also want to know, if the results are reproducible, we compared the spectrum of identical PCB.

Type 1 PCB

The center conductor of the Type 1 PCB has a width W of 73 μm and a gap S of 186 μm. As you can see the center conductor is very thin compared to the ideal dimensions of a center conductor of a PCB. This leads to a strong impedance mismatch to the 50 Ω of the print connectors. Fig. 4.2 shows the measured and by microwave office simulated S-matrix of the PCB. The transmission and the reflection show a strong oscillating behavior, because of the impedance mismatch. The same behavior is also seen in the simulation. The transmission is decreasing for higher frequency due to resistance, what is expected from the simulation, but the effect is stronger in the measured curve. The reflection is very strong ($> 10\ dB$) for frequencies around 20 GHz, this has been seen before [27] and is caused by the impedance mismatches between the printed MMPX-connector and the PCB.

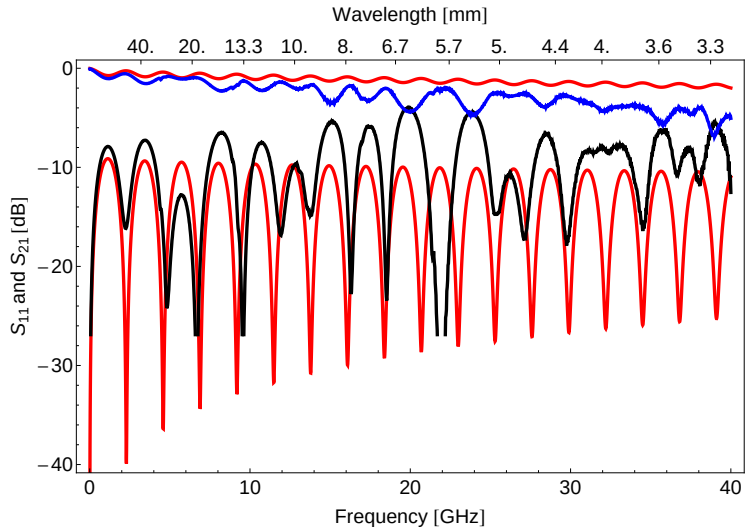

Figure 4.2: The spectrum of a Type 1 PCB. The blue curve is the transmission (S_{21}) and the black curve is the reflection (S_{11}) of the waveguide. The red curve shows the respective simulation done by microwave office

Type 2 PCB

The Type 2 PCB has a center conductor with a width W of 113 μm and a gap S of 141 μm and thus the parameters of the Type 2 PCB are nearer to the ideal PCB than Type 1 PCB. The microwave spectrum of the Type 2 PCB has been calculated and measured. The result can be seen in Fig. 4.3. The reflection is still oscillating like expected from the simulation, but not so strong anymore like in the case of the Type 1 PCB. The transmission is not oscillating anymore and it is almost equal to the simulation. The impedance mismatch between the waveguide of the PCB and the print connectors has to be decreased to lower the reflection. A plot of the S-matrix of Type 2 PCB is shown in Fig. A.1.

The print connectors are soldered to the PCB. We want to check, if the soldering is done well and reproducible. So we measure two different PCBs with the same (Type 2) geometry and compare the results. If the soldering is done well and does not effect the measurement, both measurements should give an identical result. Fig. 4.4 shows the transmission and the reflection spectrum of two identical PCB. The transmission is almost the same for both, but the reflection differ a bit for high frequencies. However the measuring results seems to be reproducible for the Type 2 PCB.

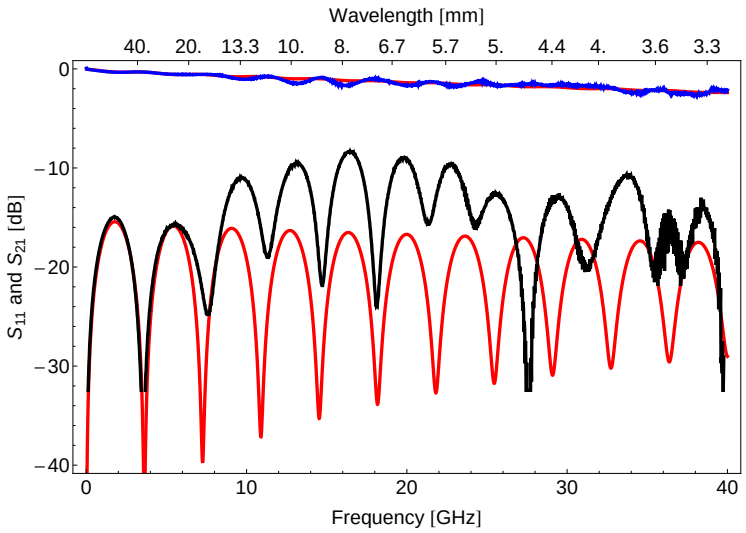

Figure 4.3: The spectrum of a Type 2 PCB used in the current experiment. The blue curve is the transmission (S_{21}) and the black curve is the reflection (S_{11}) of the waveguide. The red curve shows the respective simulation done by microwave office.

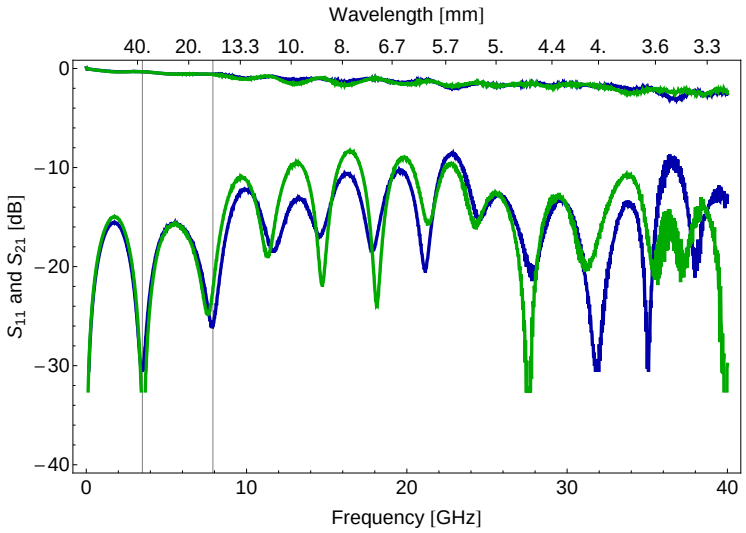

Figure 4.4: The spectrum of two identical, Type 2 PCB. The reflection and the transmission are for small frequencies nearly equal. For higher frequency the difference between the two curve is raising. The black lines mark the frequency different $\Delta f = 4.4\ GHz$ ($\Delta\lambda = 29\ mm$) of the oscillations.

Name(s)	l [μm]	Gap [μm]	C_κ [fF]	f_1 [GHz]	Q_1[1]
D0E1/D4E2	8636	4	25.3	6.84	249
O6D1/D7D2	8580	60	10.6	7.00	1184
C0CE1/C6CE2	18006	4	24.9	3.37	1206
C1CF1/C3CF2	18006	60	10.6	3.42	5554
G2B1/E1B2	7196	120	6.5	8.39	2632
G5A2/G1A2	7196	190	3.3	8.36	6895

Table 4.1: The resonator length, the length of the gap in the center conductor, the coupling capacitance determined by fitting to the measured results and the frequency and the Q-factor of the first mode for the samples used in this experiment.

4.2 Spectrum Measurements of the Resonators

In the last section the PCB was characterized. At this point we are interested in superconducting chips on the PCB (Type 2). We are starting with the most simplest resonator (just a straight waveguide) and gradually increase complexity. The samples measured in this section and their properties are shown in Tab. 4.1, in Tab. 3.1 and in Tab. B.1. The frequencies and the Q-factor of the first mode and the coupling capacitance were determined by fitting the measured data. For every resonator we measure first a chip with the same design but without a resonator gap. This chips are called "through". The transmission spectrum of the "through" is subtracted from the transmission of the resonator in order to get rid of the influences of the PCB, connector effects and the superconducting chip, only keeping the pure resonances. All measurements are made with two samples to check if the results are reproducible.

4.2.1 Small Chip Design

The simplest microwave resonator we can think of is a straight line. We have to understand this resonator in order to characterize the more complex resonators. The chips have a size of 2 $mm \cdot 9.3$ mm. We would like to measure first a "through" and just consider the difference between the transmission spectrum of the "through" and the resonators. But unfortunately the "through" was destroyed during production and therefore we cannot get rid of the influences of the PCB and connector effects. However it is possible to measure the resonance frequencies and Q-factors. But it is difficult to determined the insertion loss and therefore do the separation of internal and external Q (Eq. 2.26 and Eq. 2.26). In order to calculate the internal and external Q-factors, we take the measurement of the straight "through" chip with dimension 4 $mm \cdot 9.3$ mm (section 4.2.2). This is possible, because we expect the transmission to be very similar.

a) 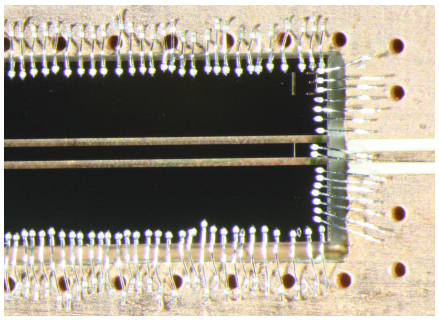 b) 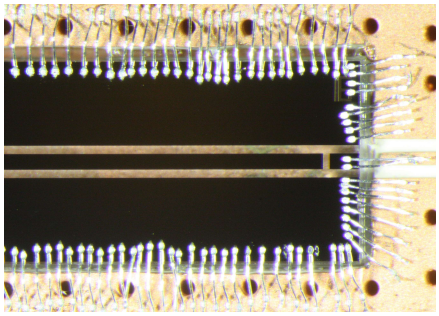

Figure 4.5: Pictures of chips in the PCB. The sample D0E1 (a) has a higher coupling capacitance C_κ than sample D7D1 (b). All the properties of the two sample can be seen in Tab. 4.1

Big Coupling Capacitance

There are four different chips of the size 2 $mm \cdot 9.3$ mm called D0E1, D4E2, O6D1 and D7D2. The first letter and number marks the name of the PCB and the second letter and number the name of the chip. Their properties can be seen in Tab. 4.1 and Fig. 4.5 shows pictures of D0E1 and D7D2. D0E1 and D4E2 have a smaller gap and therefore a bigger coupling capacitance than O6D1 and D7D2.

The measurement of the microwave spectrum of the straight resonator with a big capacitance is performed twice (D0E1 and D4E2) in a dipstick with a power of 8 dBm and an average factor of 5 (section 3.4). Fig. 4.8 shows the transmission (S_{21}) and the reflection (S_{11}) of D0E1 and D4E2 from 10 MHz to 40 GHz. (S_{12}) looks similar to (S_{21}) and (S_{11}) looks similar to (S_{11}) and therefore these two spectra are not shown. The curves of D0E1 and D4E2 look very similar up to a frequency around 30 GHz, then the spectrum becomes noisy. The transmission and the reflection show strong resonances at multiple of the frequency of the first mode at 6.84 GHz. The resonances can be clearly identified up to the fifth mode. Fig. 4.7 shows the spectrum of the first resonance (6.84 GHz) and the fitting curve to the data by a Lorentzian function (see Eq. 2.20) with a Q-factor of 249. The spurious resonances, which appear for $f > 20$ GHz, could be caused by other resonators for example between the transmission line and the chip edge or between the resonator gap and bonds on the center conductor.
We learn, that the measurement of the spectrum of this sample is reproductive for frequencies up to 30 GHz and the resonances are at the expected frequencies. Every resonances is fitted and the Q-factors, the attenuation constants α and the resonance frequencies f_n are extracted (Tab. B.1).

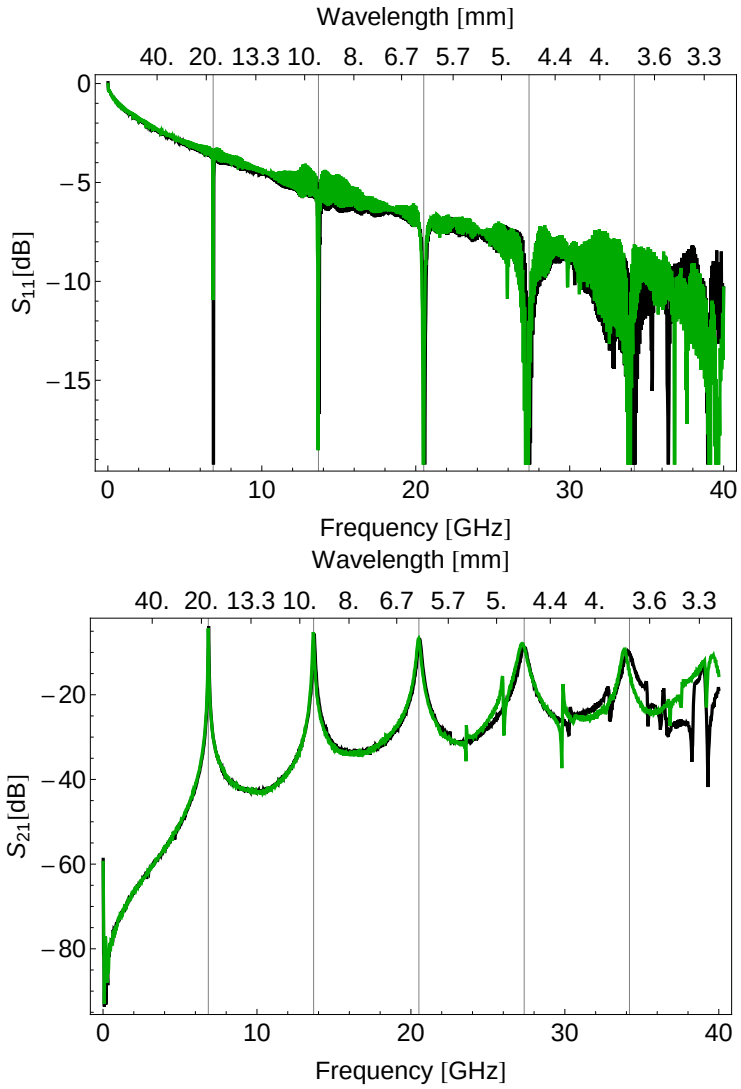

Figure 4.6: The microwaves spectrum of D4E2 (black) and D0E1 (green). The two sample have the same geometry (see Tab. 4.1) and has therefore a similar spectrum. The black, dotted lines mark multiple of the first resonance frequency at 6.84 GHz

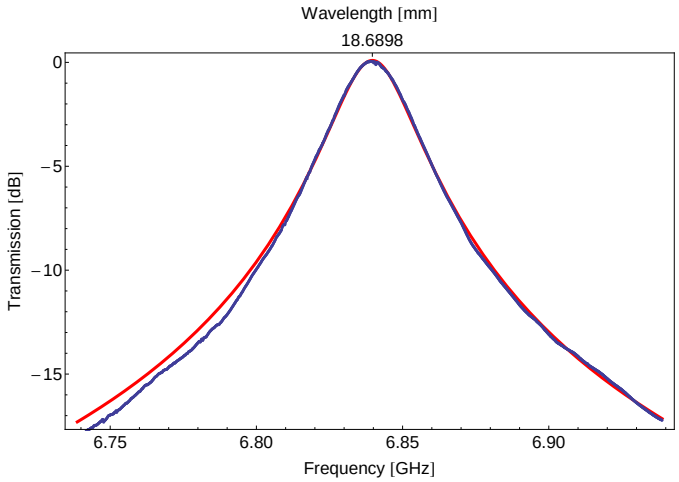

Figure 4.7: The transmission spectrum of D0E1 around the first resonance. The blue line is the measurement result and the red line is a Lorentzian function (see Eq. 2.20) with $f_0 = 6.84\ GHz$ and $Q = 249$.

The goal of the experiment is to find resonances with a high Q-factor. But in the interesting range around the fourth resonances (27.23 GHz) the Q-factor is only 52. The Q-factor is mainly determined by Q_{ext}, which is a result of the strong coupling capacitance. Therefore the next measurement is done on a weaker coupled resonator.

Small Capacitance

The samples O6D1 and D7D1 (see Fig. 4.5) have a bigger gap and therefore the smaller coupling capacitance than the samples D0E1, D4E2 (see Tab. 4.1). The spectrum of O6D1 and D7D1 look very similar up to a frequency of 30 GHz like in the measurement of D0E1 and D4E2 before (Tab. B.1). This measurement shows, that also for a weaker coupled resonator the measurement is reproducible up to a frequency around 30 GHz.

Fig. 4.8 compares the spectrum of D7D1 (small capacitance) and D4E2 (big capacitance). The resonance frequencies are shifted by the difference in the coupling capacitance C_κ (Eq. 2.18 and Eq. 2.19). The resonances are at the expected frequencies (multiple of the frequency of the first mode at 7.01 GHz). The resonances can clearly be seen up to the fifth resonances at 34.79 GHz, which has a Q-factor of 421.

The resonances are at the expected positions and not so wide as in the case before. In the next section the spectra are simulated and the calculated and measured Q-factors are compared for the small and the big capacitance.

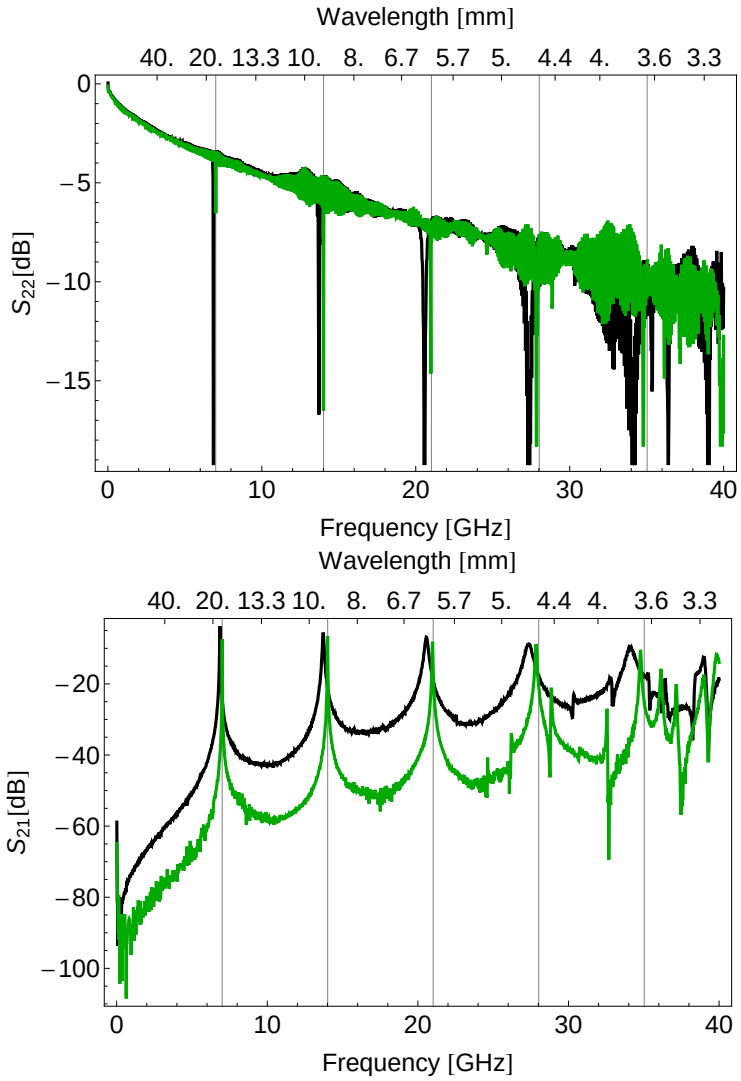

Figure 4.8: The microwaves spectrum of D4E2 (black) and D7D1 (green). D7D1 has a smaller coupling capacitance than D4E2 (see Tab. 4.1) and has therefore bigger Q-factors. The black, dotted lines mark multiple of the first resonance frequency of D7D1 at 7.01 GHz

There are still spurious resonances and some of them repeat in both measurements (Fig. 4.8)

Simulation and the Q-factors

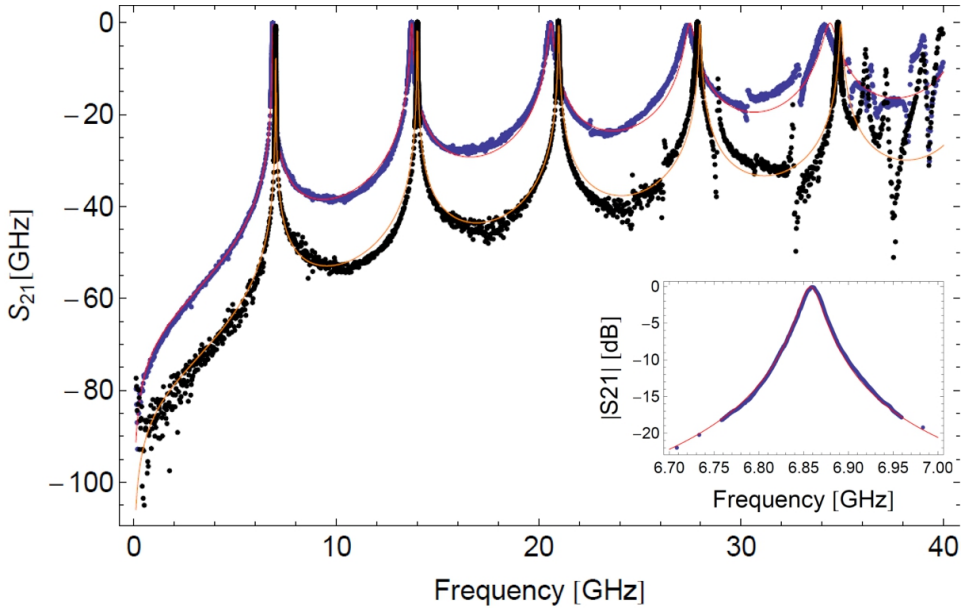

Figure 4.9: The transmission spectrum of D4E2 measured (blue) and simulated (red) with the ABCD-matrix analysis and the transmission spectrum of D7D1 measured (black) and simulated (orange) with the ABCD-matrix analysis. The fitting parameters can be seen in Tab. B.2. The insert shows a zoom to the first peak of D4E2

The spectrum of the coplanar waveguide can be simulated by an ABCD-matrix analysis [13]. The measured spectrum of the resonator is fitted in simulation with the coupling capacitance C_κ and the propagation constant γ as a parameter. The coupling capacitance and the propagation constant determined with this simulation can be seen in Tab. 4.1 and Tab. B.2. Fig. 4.9 shows the simulated and the measured microwave spectrum of D4E2 and D7D1. It can be seen, that the simulations fit the measured data well for all resonances. Only the spurious modes lead to a deviation from the simulation.

The coupled capacitance C allows us to calculate the simulated external Q-factors, the propagation constant $\gamma = \alpha + i \cdot \beta$ allows to calculate the simulated internal Q-factor. With Eq. 2.25 also the Q-factor and with Eq. 2.24 g can be determined. With Eq. 2.27 the resonance shift, caused by C^* and

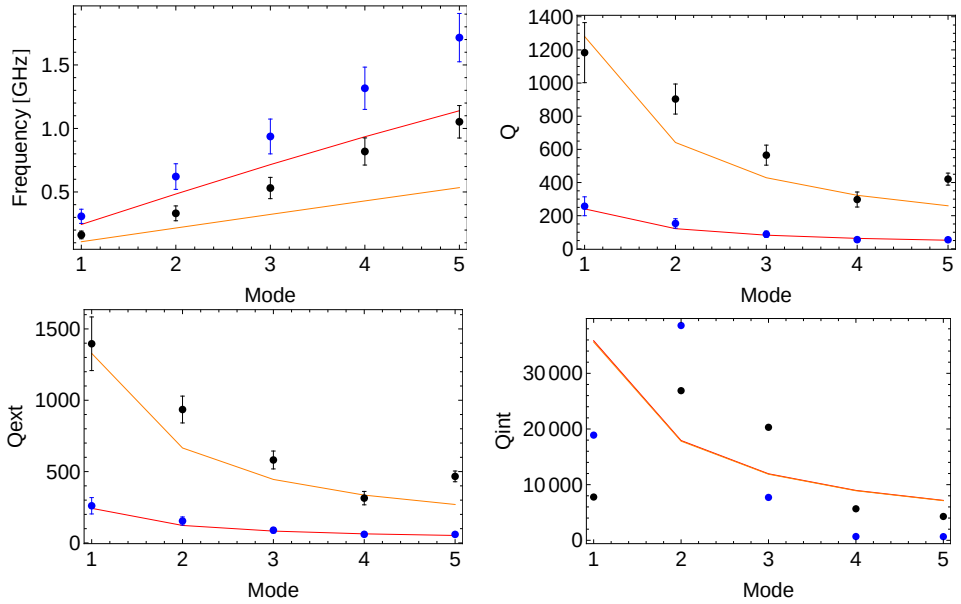

Figure 4.10: The simulated and the measured resonance shifts caused by C^* and L_l^k, Q-factor, internal Q-factor and external Q-factor. The simulated (red) line and the measured (blue) points of D4E1 are compared to the simulated (orange) line and measured (black) points of D7D1.

L_l^k (The frequency calculated by Eq. 2.27 subtracted from the frequency calculated by Eq. 2.19), can be simulated as well. All this simulations and the measured values are compared in Fig. 4.10. The Q-factor is for both samples mainly determined by the external Q-factor. Both samples are therefore still overcoupled, for example g is 5.9 for the first mode of O6D1(Tab. B.1). The Q-factor (and therefore also the external Q-factor) fits well for sample D4D7. The simulations of the frequency shifts and the internal Q-factors differ more from the measured values, but show the right mode dependence. The design of the waveguide has not been changed and therefore the simulated internal Q-factor of the resonator are nearly the same for D4E1 and D7D1. The errors are determined by the Gaussian law of error propagation [28].

The simulation and the measured results give approximately equal results for the Q-factors, the frequency shift of the resonances and for the external Q-factor and the two curve match for frequency lower than 35 GHz. The spectrum for a straight resonator seems to be completely understood up to the distinguish of the Q_{int} and Q_{ext}. It would help more, if there were more modes, which can be simulated and measured. Since the resonator here has a length of $7mm$, there are only five modes in the range of 10 MHz to 40 GHz. In order to raise the number of mode, we use a bigger chip design

($4.3\ mm \cdot 9.3\ mm$ instead of $2\ mm \cdot 9.3\ mm$) to make longer resonators.

4.2.2 Big Chip Design

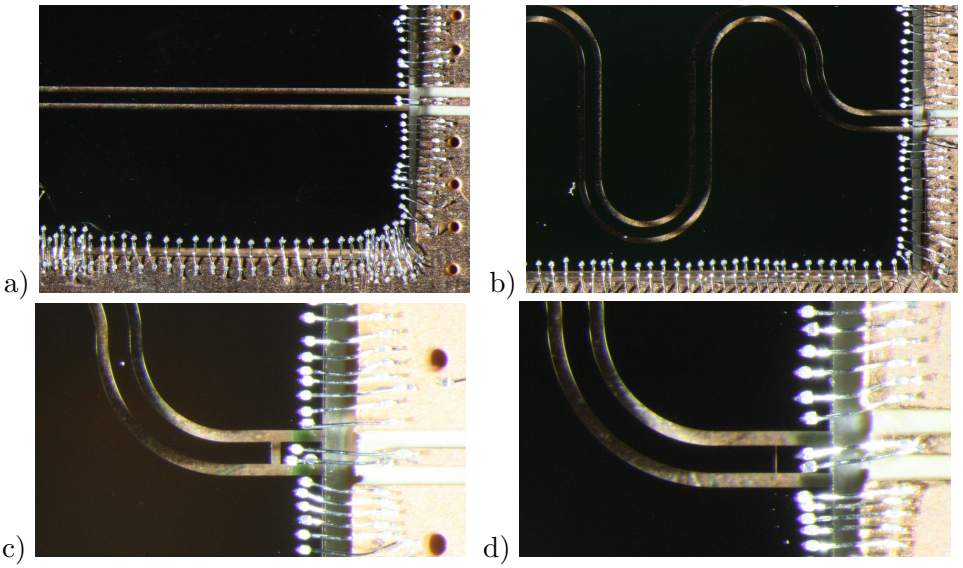

Figure 4.11: Picture of samples with the big chip design ($4.3\ mm \cdot 9.3\ mm$). a) shows the straight "through" (C4I1). A curved "through" (C5CD1) is shown in b). Sample C3CF2 (c) and C0CE1 (d) are curved resonators with different capacitance. The properties of C3CF2 and C0CE1 are described in Tab. 4.1.

In the last section the resonance frequencies and the Q-factors of a resonator with a length about 7 mm be measured and simulated. The number of modes was limited by the maximal frequency of 40 GHz. In order to extend the number of modes, we use now a bigger chip design ($4.3\ mm \cdot 9.3\ mm$), which allows to have longer resonators with a curved waveguide. First we measure a "through" and then a resonator with a small and big capacitance. Fig. 4.11 shows picture of the chips measured in this section.

"Throughs" and Fitting Curves

A "through" is a chip, which has a coplanar waveguide but no resonator. The TOSM calibration only gets rid of the influences of the coaxial cable and therefore the transmission line of the "through" is subtracted from the transmission of the resonator to get rid of the influences of the PCB and connector effects. Two different "throughs" ($4.3\ mm \cdot 9.3\ mm$) are measured. Fig. 4.11 a) shows a picture of the first sample called C4I1. It is a straight through, which was used to calibrate the PCB in the last section. The second

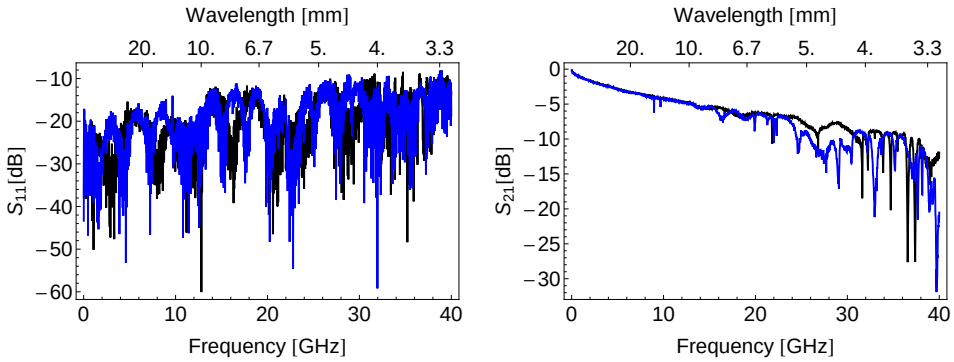

Figure 4.12: Transmission and reflection spectrum of C4I1 (straight through, black) and C5CD1 (curved through, blue). Although the two samples have a different length, they look similar. Especially the transmission for frequency up to 20 GHz.

sample called C5CD1 can be seen in Fig. 4.11 b) and is a curved "through" with a waveguide length about 18600 μm. The microwave transmission and reflection spectrum of C4I1 and C5CD1 are compared in Fig. 4.12. Although the two transmission line have a different resonator lengths, they look similar. We see, that the blue curve (C5CD1) has a lot more resonances for $f > 20\,GHz$. There was a second curved "through" (called C5CD2) with the same geometry like C5CD1, which was used to test the reproducible of the measurement. Both curves look similar up to a frequency of 30 GHz (Tab. A.2).

Since for high frequencies (>20 GHz) the transmission spectrum becomes very noisy, we run into the problems of generally spurious resonances, if we now subtract the transmission curve of the "through" from the transmission curve of a resonators. In order to avoid this, the transmission curve of the "through" is fitted for frequencies below 20 GHz with the ansatz: [29]

$$y(f) = -a \cdot f^b \tag{4.1}$$

The fitting curve of C4I1 is given by $a = 1.20763$ and $b = 0.5666504$ and was used in the last section to calibrate the resonators on the small chips ($2\ mm \cdot 9.3\ mm$). The measurement and the fitted transmission curve of C5CD1 is shown in Fig. 4.13. The fitting parameters are: $a = 1.13636$ and $b = 0.582482$. This fitting function is subtracted from all the big chips ($4.3\ mm \cdot 9.3\ mm$) transmission curve in the following section.

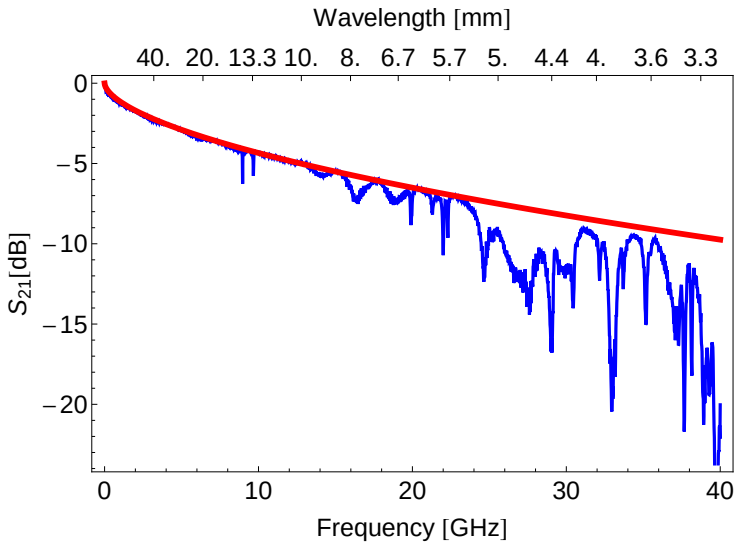

Figure 4.13: The transmission of C5CD1 (curved through) is first measured (blue) and then it is fitted (red) by the ansatz $y(\nu) = -a \cdot \nu^b$ ($a = 1.13636$, $b = 0.582482$) for frequencies below 20 GHz. The fitting curve match the data nearly perfect in the fitting range.

Big Capacitance

There are four different samples with a resonator on a big chip (4.3 $mm \cdot$ 9.3 mm). Two of them, called C6CE2 and C0CE1, have a small gap and therefore a big coupling capacitance C_κ. The other two, called C3CF2 and C1CF1, have small coupling capacitance C_κ. Picture of C3CF2 and C0CE1 can be found in Fig. 4.11 c) and d). The properties of the samples can be found in Tab. 4.1. The transmission and reflection spectrum of the C6CE2 and C0CE1 (big capacitance) can be seen in Fig. 4.14. The two curve look similar up to a frequency of 25 GHz. All the resonances have a multiple of the ground mode frequency (3.37 GHz). We found resonances up to 27 GHz (8^{th} mode) for C6CE2 and resonances up to 33 GHz (11^{th} mode) for C0CE1. Resonances with higher frequencies could not be seen.

The measurement is reproducible up to frequencies of 25 GHz. The higher modes, that could be defined, are at the expected frequencies. The Q-factor of the first mode is 1206. In the interesting range (section 3.1) of 27 GHz the Q-factor is only 27 (Tab. 4.1). Since we are interested in higher Q-factors, the next measurement is performed with resonators with weaker coupling capacitance.

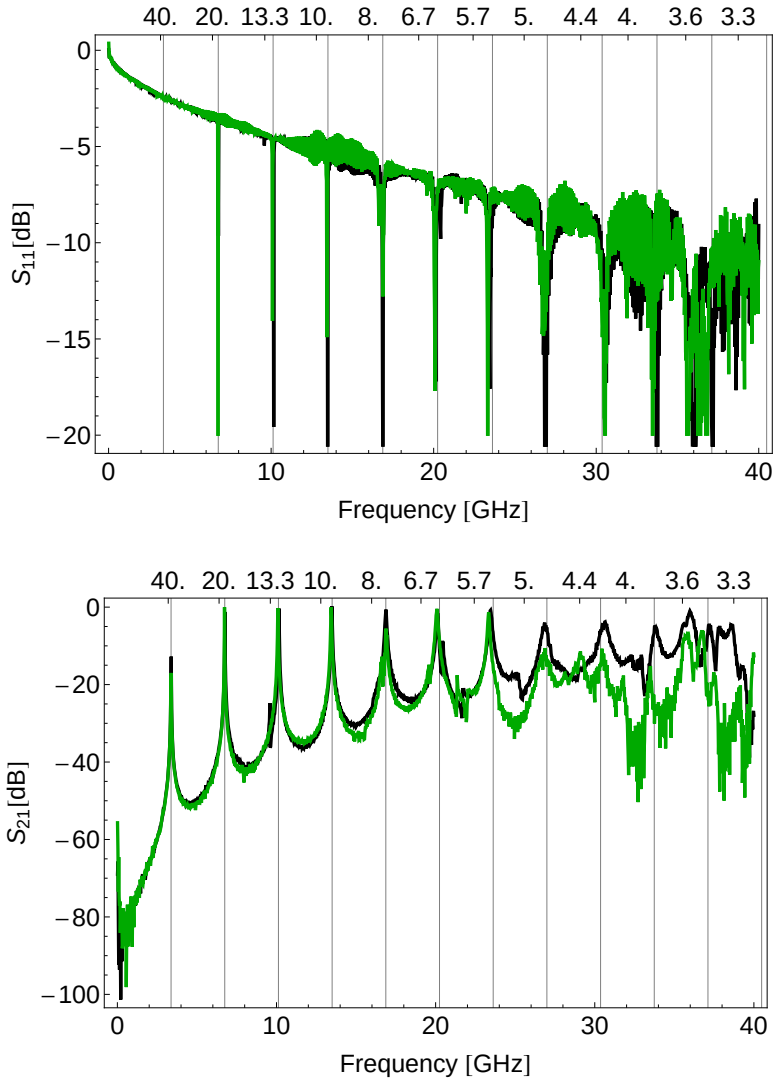

Figure 4.14: Transmission and reflection spectrum of C0CE1 (curved, big capacitance, black) and C6CE2 (curved, big capacitance, green). The two samples have the same geometry and look similar up to 30 GHz. The resonances are at the expected frequencies. The black, dotted lines show multiples of the ground mode frequency of 3.37 GHz.

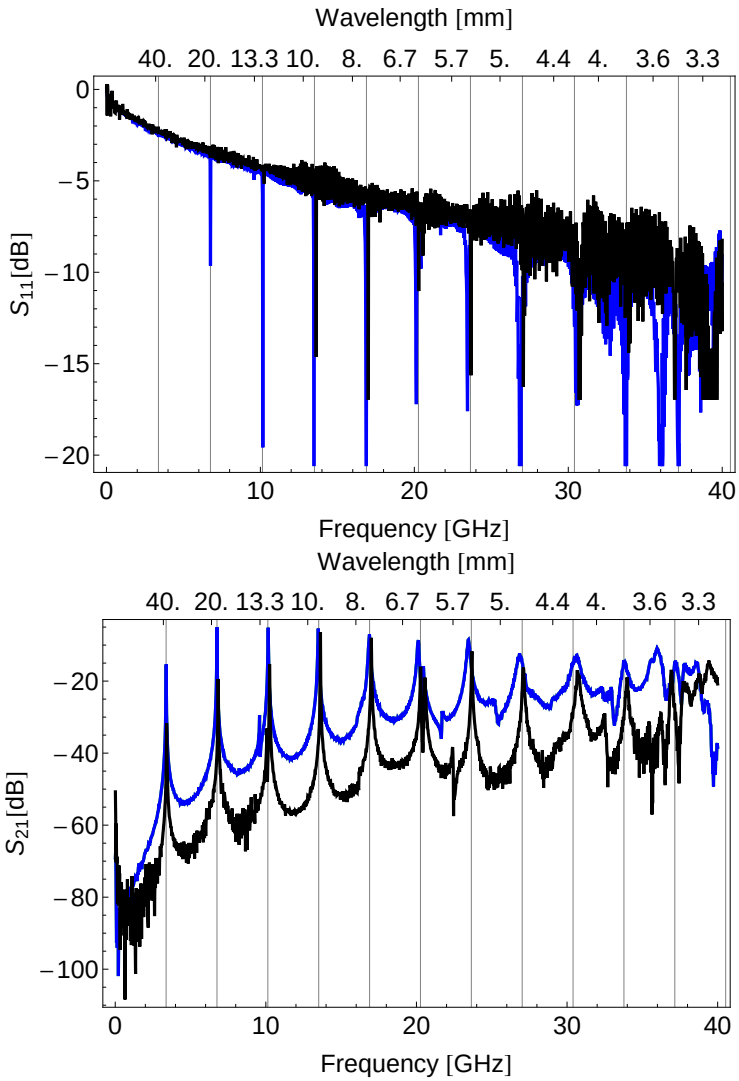

Figure 4.15: Transmission and reflection spectrum of C1CF1 (curved, small capacitance, black) and C0CE1 (curved, big capacitance, blue). The resonance frequencies are nearly the same and can be seen up to a frequency of 34 GHz. The Q-factors of C1CF1 are bigger than the Q-factors of C0CE1. The black, dotted lines mark multiples of the ground mode frequency (3.37 GHz) of C0CE1 .

Small Capacitance

We want to couple microwave photons with a frequency around 27 GHz to the Rydberg atoms. The Q-factors of the samples C6CE2 and C0CE1 (big capacitance) are low for such high modes. Therefore we measure the transmission and reflection of C3CF2 and C1CF1, which have a bigger gap and therefore a smaller capacitance (Tab. 4.1). The spectrum of C3CF2 and C1CF1 look similar up to a frequency of 34 GHz and are therefore reproducible (Tab. A.3). The resonances can be seen in both samples up to this frequency (10^{th} mode) and the resonances are at the expected positions.

The spectrum of the sample C3CF2 (small capacitance) and C0CE1 (big capacitance) are compared in Fig. 4.15. The resonances are nearly at the same position. But C3CF2 has bigger Q-factors and less transmission off-resonance. For example, the Q-factor of the first mode of sample C3CF2 is 5554 and at the interested frequency of 27 GHz a Q-factor of 114. In the next section we have closer look at the Q-factors.

Simulation and the Q-factors

The four samples C1CF1, C3CF2 (small capacitance), C6CE2 and C0CE1 (big capacitance) are also simulated by an ABCD-matrix analysis (section 4.2.1, [13]). The coupling capacitance is determined by fitting the ABCD-matrix analysis to the measured spectrum. The fitted coupling capacitance C_κ can be found in Tab. 4.1. Fig. 4.16 compares the spectrum of the simulation with the spectrum of the measurement for the sample C3CF2 (small capacitance) and C0CE1. The fitting parameter are in Tab. B.2. The two curves match nearly perfect for frequency up to 30 GHz. At higher frequencies the measured curve becomes noisy. This is also true for the other two sample (C6CE2 and C1CF1) not shown in the figure.

The coupling capacitance C_κ allows us again to calculate the simulated internal and external Q-factors and with Eq. 2.25 also the Q-factor. The resonance shift, caused by C^* and L_l^k (Eq. 2.18), can be simulated like before in section 4.2.1 with Eq. 2.27. All these simulations and the measured values are compared in Fig. 4.17. The Q-factor is in both samples mainly determined again by the external Q-factor. Both samples are therefore still overcoupled (e.g. $g = 9$ for the first mode of C3CF2, Tab. B.1). The simulation of the Q-factor and of the external Q-factor match well with the measured points. The frequency shifts and the internal Q-factor show the right mode dependence. The errors are determined by the Gaussian law of error propagation [28].

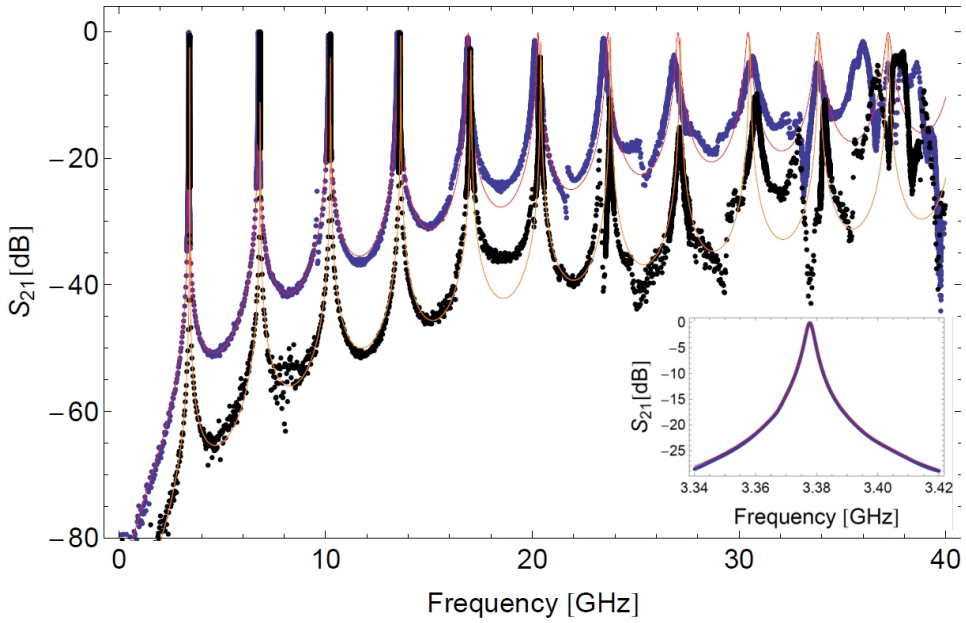

Figure 4.16: The transmission spectrum of C0CE1 measured (blue) and simulated (red) with the ABCD-matrix analysis and the transmission spectrum of C3CF2 measured (black) and simulated (orange) with the ABCD-matrix analysis. The simulations are nearly perfect for frequency up to 30 GHz. The fitting parameters can be seen in Tab. B.2. The insert shows a zoom to the first peak of C0CE1.

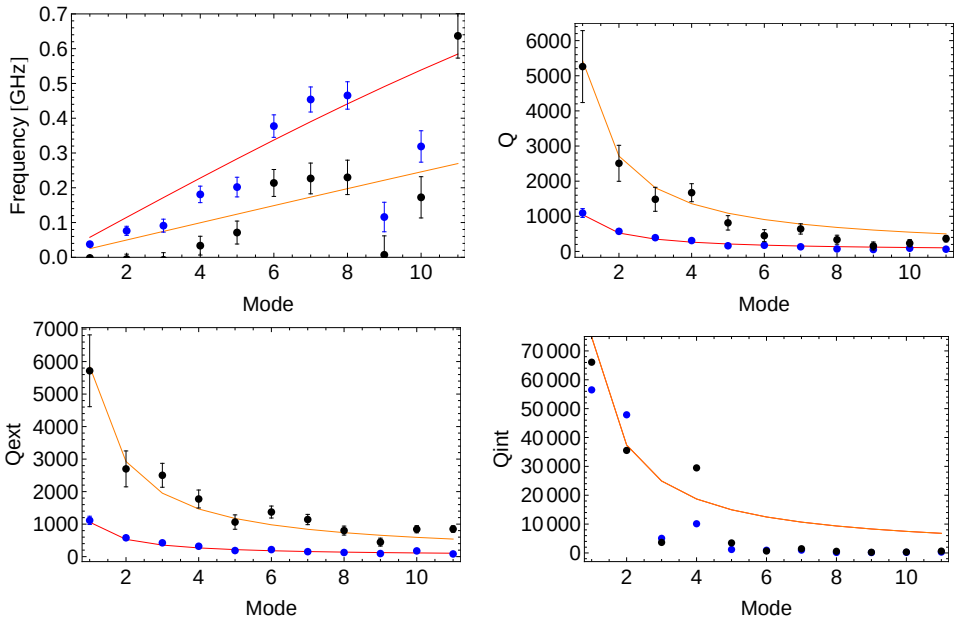

Figure 4.17: The simulated and the measured resonance shifts caused by C^* and L_l^k, Q-factor, internal Q-factor and external Q-factor. The simulated (red) line and the measured (blue) points of C0CE1 are compared to the simulated (orange) line and measured (black) points of C1CF1.

The measurement were made to have more modes for the simulation and to become a better understanding of the spectrum. The simulated curve matched with the measurements results and the Q-factors are understood now. The problem of the measurement is still the low external Q-factor, which with Eq. 2.27 also decreases the Q-factor. Therefore the next samples will be even weaker coupled than the samples before.

4.2.3 Final Chip Design

a) 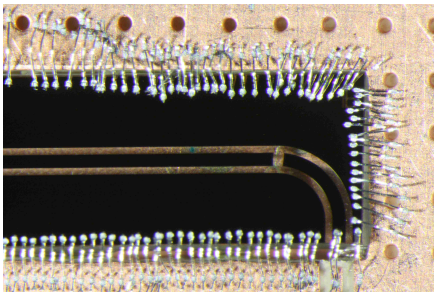 b) 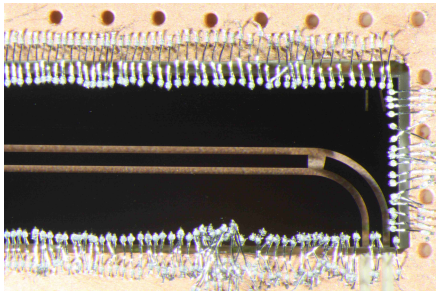

Figure 4.18: Pictures of chips stuck crossways in the PCB. The sample G2B1 (a) has a higher coupling capacitance C_κ than sample G1A1 (b). All the properties of the two sample can be seen in Tab. 4.1

The goal of the experiment is to use the Rydberg atoms as RAM by interacting with the photons in the waveguide resonator. Since the Rydberg atoms will fly crossways with respect to the long edge of the PCB, a long waveguide will be needed, which also lies crossways. This is only possible, if the chip lies crossways as well. There are six samples with a crossways lying chip in this experiment (G3D1, G6D1, G2B1, E1B2, G1A1 and G1A2). Picture of G2B1 and G1A1 can be seen in Fig. 4.18. We measure again first the transmission of a "through" (G3D1 and G6D2) and than subtract it from the transmission of the resonators in order to get rid of the influences of the PCB. The resonators used before are all overcoupled and have therefore low Q-factors. This time the coupling capacitance of the samples are small compared to the samples before. There are four samples with two different coupling capacitance, G2B1, E1B2 (big capacitance) G1A1 and G1A2 (small capacitance). Tab. 4.1 shows the properties of them.

"Throughs" and Fitting Curve

The samples G3D1 and G6D2 are two curved through, which have the same geometry like G2B1, E1B2, G1A1 and G1A2 but with no resonator on the transmission line. The microwave transmission of the two "throughs" look

similar (Tab. A.4). The transmission is fitted (section 4.2.2) by the fitting ansatz :

$$y(f) = -a \cdot f^{b} \tag{4.2}$$
$$y(f) = -2.851 \cdot f^{0.5588507}. \tag{4.3}$$

This function is subtracted from the transmission spectrum of every curved chip resonator.

Resonators

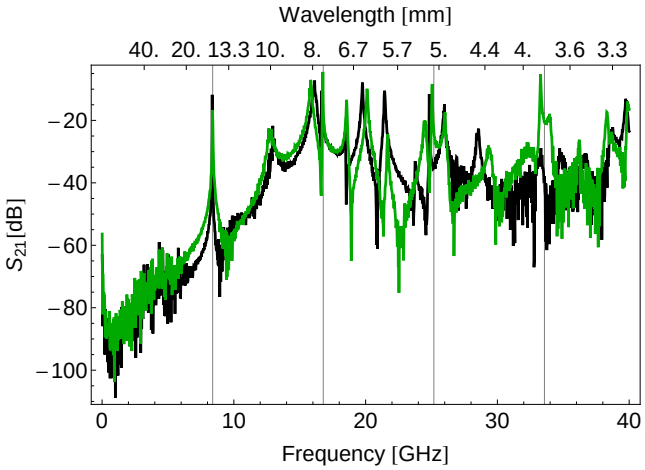

Figure 4.19: The microwaves transmission of G1A1 (black) and G2B1 (green). G1A1 have a smaller coupling capacitance as G2B1 (see Tab. 4.1). The black, dotted lines mark multiples of the first resonance frequency at 8.39 GHz

We have reached the final chip design, where the resonators are crossways to the PCB. There were two different kind of resonators, G2B1/E1B2 (big capacitance) and G5A2/G1A2 (small capacitance). The properties of the four samples can be seen in Tab. 4.1. The gaps, which define the resonators, are bigger than in the measurements before. Therefore even the samples G2B1/E1B2 have a smaller capacitance than all the other resonators before. We hope, that the resonances are undercoupled and thus have higher Q-factors.

Fig. 4.19 shows the microwave spectrum of the samples G1A1 (big capacitance) and G2B1(small capacitance). The resonances are at the expected frequencies, but the spectra are very noisy for frequencies higher

than 10 GHz. However the resonances can be seen up to a frequency of 25 GHz. This is due to a) the small chip size and b) the curvature of the transmission line, that enhances coupling out of the waveguide.

Simulation and the Q-factors

The spectrum of the samples is also simulated by the ABCD-matrix analysis like in the measurements before. Fig. 4.20 compares the simulated and the measured transmissions of the samples G2B1 and G1A1. The fitting parameters can be seen in Tab. B.2. The simulation do not match to the measured data in the off-resonance area like it did in the measurements before.

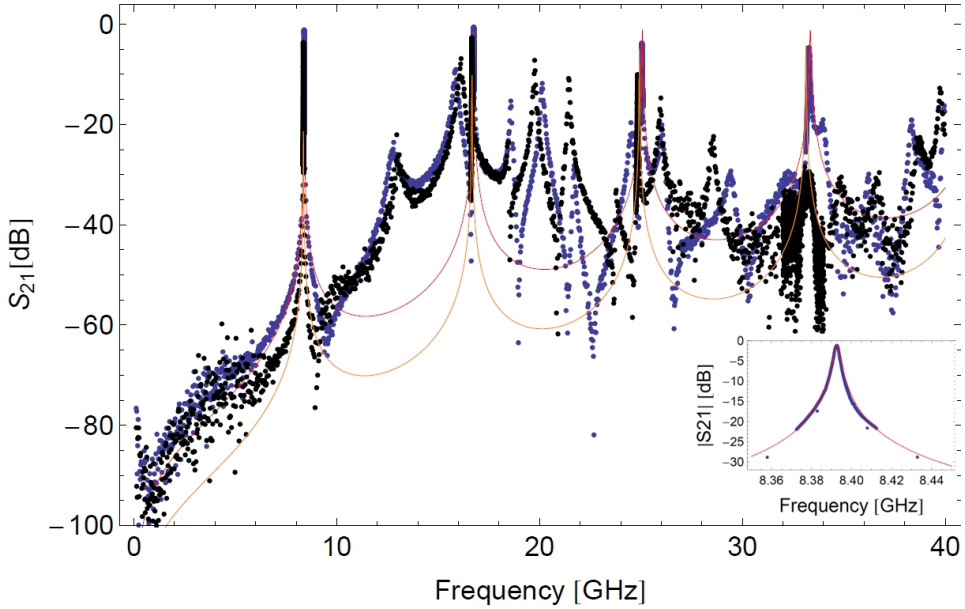

Figure 4.20: The transmission spectrum of G2B1 measured (blue) and simulated (red) with the ABCD-matrix analysis and the transmission spectrum of G1A1 measured (black) and simulated (orange) with the ABCD-matrix analysis. The simulation is well at the resonance frequency. Off-resonance the simulation differs from the measured data. The fitting parameters can be seen in Tab. B.2. The insert shows a zoom to the first peak of G2B1.

The measured and simulated Q-factors and the resonance shifts, caused by C^* and L_l^k (The frequency calculated by Eq. 2.27 subtracted from the frequency calculated by Eq. 2.19), can be seen in Fig. 4.21. The external Q-factors has been increasing compared to the measurement before. But it is still lower than the internal Q-factor. The system is therefore still

overcoupled (e.g. $g = 2$ for the first mode of G1A1, Tab. B.1). The errors are again determined by the Gaussian law of error propagation [28].

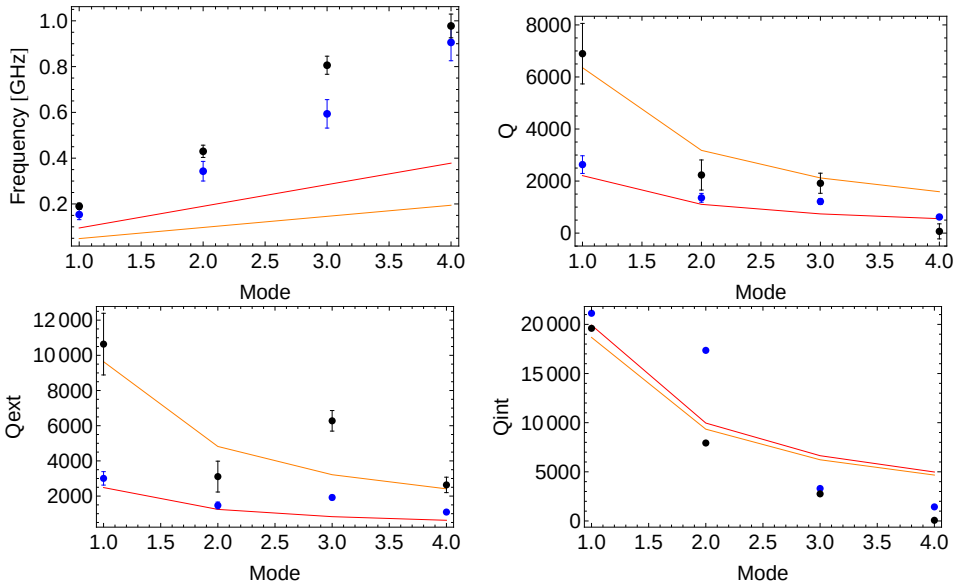

Figure 4.21: The simulated and the measured resonance shifts caused by C^* and L_l^k , Q-factor, internal Q-factor and external Q-factor. The simulated (red) line and the measured (blue) point of G2B1 are compared to the simulated (orange) line and measured (black) points of G1A1.

The resonators of the final chip design are weakly coupled and the Q-factors are on the required order Tab. B.1. But the resonator is still overcoupled what means, that the capacitance between the resonator and the transmission line should even be lowered.

4.3 Kinetic Inductance

In previous experiments Nb was used as superconducting metal on the chip. The novelty in this experiment is to use NbTiN, which has a higher critical temperature T_c. Therefore we expect to measure higher Q-factors. A side effect of the higher critical temperature is the kinetic inductance, as discussed in section 2.4.4. In case of NbTi the kinetic inductance was negligible compared to the magnetic inductance. Due to the higher critical temperature of NbTiN the ratio between the kinetic and magnetic inductance is around 0.04 at 4 K (Fig. 2.8) for this sample geometry and is therefore not negligible anymore. The effect gets even more pronounced of smaller geometries. We are interested to understand the kinetic inductance in NbTiN. So

we tried to increase the kinetic inductance , firstly by changing the geometry of the waveguide and secondly by changing the temperature.

4.3.1 Geometry-Dependence

The kinetic inductance depends on the London penetration depth, which depends on temperature, and the geometry of the waveguide. The thinner the waveguide is, the higher is the kinetic inductance and thus we used a chip with a thin waveguide. The chips are called B0RG1 and B0RG2 and are on the same PCB and have the same properties, which can be seen in Tab. 4.2. A picture of B0RG1 is show in Fig. 4.22.

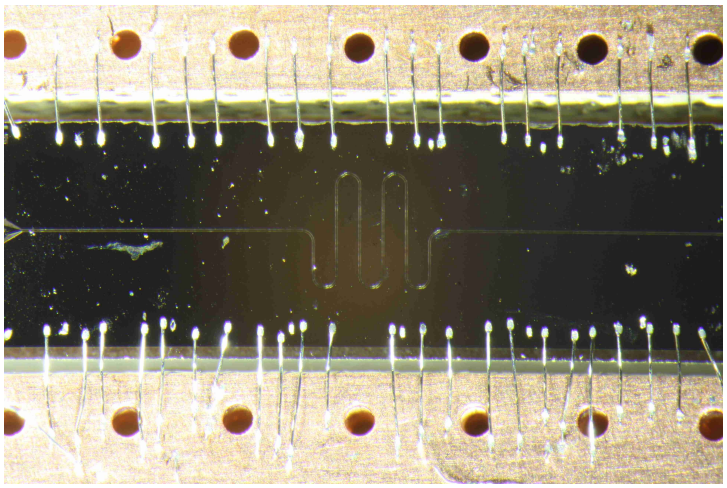

Figure 4.22: Picture of the sample B0RG1. The waveguide is thinner than before and therefore the kinetic inductance is important in this sample. The properties of this sample can be seen in Tab. 3.1

The chips B0RG1 and B0RG2 consist of the same material, NbTiN, like the chips before. But the kinetic inductance is stronger in the samples B0RG1/B0RG2 because of their geometry. Fig. 4.23 shows the temperature dependence of the kinetic inductance divided by magnetic inductance for the geometry of the samples B0RG1 and B0RG2. The measurement is made in a liquid helium dewar and therefore the temperature is $4,2\ K$ like in the measurements before. At this temperature the kinetic inductance is five times stronger then the magnetic inductance. Therefore the resonance frequency is expected to be shifted down as a result of the kinetic inductance

The resonance frequency of a resonator is given by Eq. 2.19. With a length $l = 10.17\ mm$ and a dielectric constant $\epsilon_{eff} = 5.9$ the first resonance

S	l	$\mu(0)$	C_l
10 μm	10.175mm	$2.23861 \cdot 10^{-7}$ m	$1.68945 \cdot 10^{-10}$ F

W	ϵ_{eff}	Z_0	L_l^m
4 μm	5.9	47.8 Ω	$3.85031 \cdot 10^{-7}$ H

Table 4.2: The properties of the NbTiN transmission line used for measure the shift of the first resonances by the kinetic inductance . The meaning of the notation can be seen in Fig. 2.4 and in section 2.4.2. The parameters, which only depend on the material are the same as in Tab. 3.1.

is expected at 6.08 GHz (Fig. 4.24). The resonance frequency is shifted down to 5.0 GHz

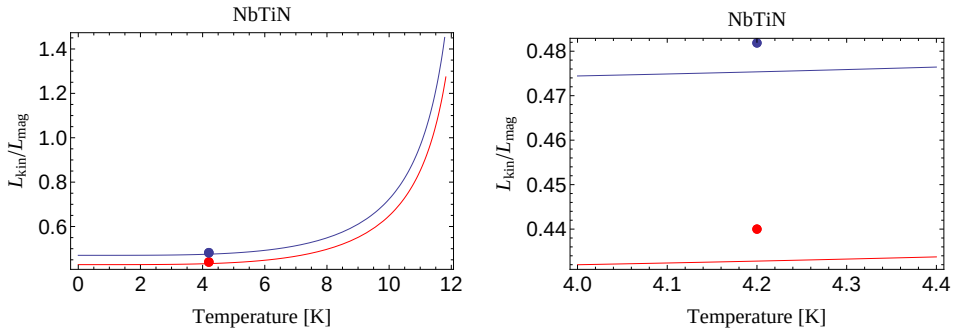

Figure 4.23: The temperature dependance of the kinetic inductance divided by magnetic inductance for NbTiN ($T_c = 13.1$ K) for the geometry of sample G2B1 ($w = 160$ μm, $s = 80$ μm, $d = 150$ nm and $\rho(T_c) = 67 \cdot 10^{-8}$ $\Omega \cdot m$) in blue and for the geometry of sample B0RG1 ($w = 160$ μm, $s = 80$ μm, $d = 150$ nm and $\rho(T_c) = 67 \cdot 10^{-8}$ $\Omega \cdot m$) in red a) from zero kelvin to the critical temperature and b) near to the boiling point of Helium ($4,2$ K). The values of G2B1 are scaled by a factor of 10

The kinetic inductance could have a strong influence on the spectrum of a waveguide. In some materials and waveguide geometry it can be neglected compared to the magnetic inductance, but in thinner waveguide it is the major part of induction. In the next chapter also the temperature dependent of the kinetic inductance is investigated.

4.3.2 Temperature-Dependence

The kinetic inductance shows a strong temperature dependence (Eq. 2.34). At a temperature of 4.2 K the kinetic inductance is just 4 % of the total induction L_l, but can not be neglected. Therefore we are interested in an-

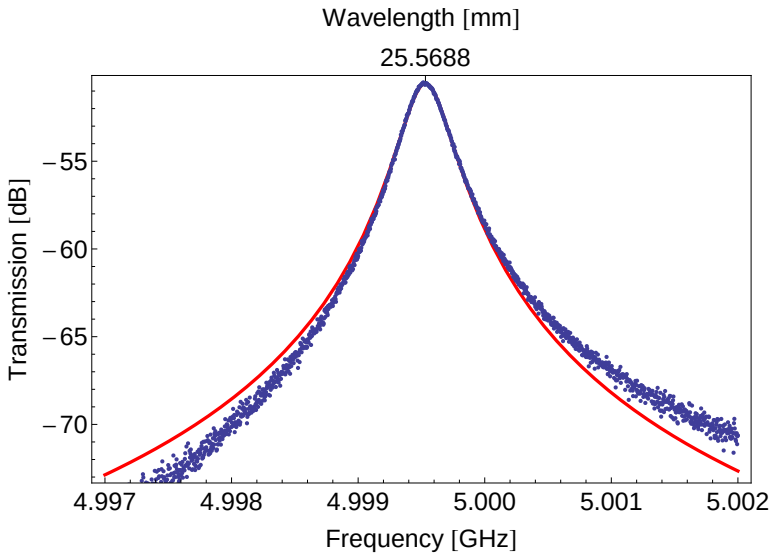

Figure 4.24: The first resonance of Sample B0RG1. The resonance is shifted down by the kinetic inductance. The red line is the lorentzian fitting curve.

alyze the kinetic inductance in NbTiN by measuring the spectrum of the Sample G5A2 (final chip design, small capacitance, see Tab. 4.1) for different temperatures. The temperature dependence measurement is made like described in section 3.3.3. We expected the frequency of the first resonances to decreasing as a function of the temperature.

Fig. 4.3.2 shows the frequency of the first resonance of sample G5A2 as a function of the temperature. The black points are the frequencies of the first resonance determined by fitting to measurement results by a lorentzian function. The blue line shows the expected temperature dependence calculated by Eq. 2.19 and the temperature dependence of the kinetic inductance (Fig. 2.8). The blue line is decreasing as a function of the temperature as a result of the increasing kinetic inductance. The black points are near to the expected values and show the same temperature dependence.

The calculated temperature depends of the kinetic inductance from Fig. 4.3.2 is in a good agreement with the measured values. The kinetic inductance seems therefore to be understood. For small temperature (smaller than 5 K) θ_λ is near to 1 and the kinetic inductance is constant but finite. And therefore it can not be neglected in NbTiN and with our chip geometry at any temperature.

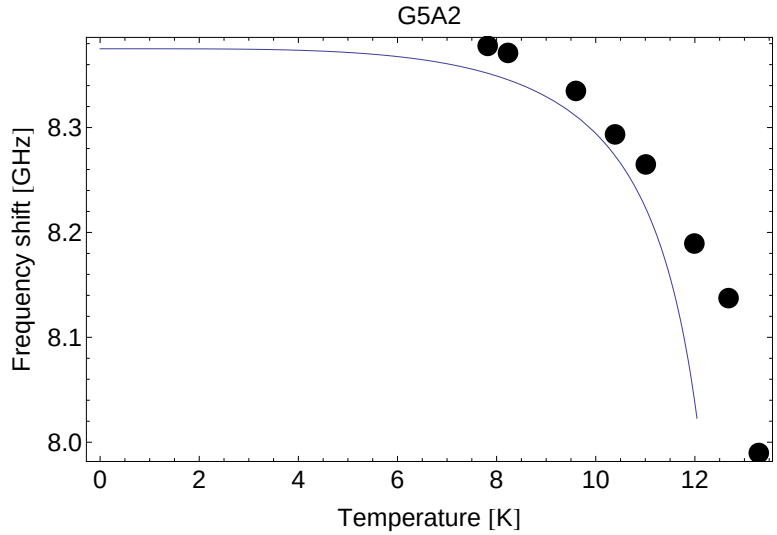

Figure 4.25: The frequency of the first resonance of sample G5A2 as a function of the temperature. The black point are measurement results and the blue line is the expected temperature dependent as a result of the kinetic inductance.

Chapter 5

Conclusion

5.1 Summary

The goal of the experiments in this thesis was to characterize coplanar microwave resonators made from NbTiN. We intended to characterize the frequency shifts and the Q-factors of the resonances (Fig. 4.10, Fig. 4.17 and Fig. 4.21), the propagation constant γ (Tab. B.2), the coupling capacitance C_κ (Tab. 4.1) and the kinetic induction (section 2.4.4 and section 4.3). If successful, this is an important step toward interfacing microwave photons in a NbTiN resonator with Rydberg atoms to use the system as a RAM of a quantum computer (section 2.3) with circuit-QED-processor .

Fabricating and measuring every sample geometry at least twice, the accuracy of the fabrication method could be tested. In almost all of the measurement the two samples show similar results (Tab. B.2) and thus the lithography, the gluing and the manual bonding (section 3.1.2) were well done. This was checked for all samples.

The PCBs used in these experiments had fabrication errors (section 4.1). Since we had two different geometry of the PCBs (Type 1 and 2), we compared the measured and simulated spectra of Type 1 and Type 2 PCBs (Fig. 4.2 and Fig. 4.3) and we could determine, that the impedance match (Eq. 2.9) is better in the new Type 2 PCBs, but still differs from the ideal impedance of 50Ω, leading to reflection.

In a next step we measured and simulated straight microwave resonators on small chips ($2\ mm \cdot 9.3\ mm$) with small and a big coupling capacitances. The simulated spectrum matches the measurements well up to the fifth resonance at 34 GHz (Fig. 4.9 and Fig. 4.10) and we could obtain the fitting parameters (Tab. B.2). The resonators are strongly overcoupled ($g = 5.9$ for the first mode of O6D1)

In order to check if we understand the theory, we measured and simulated longer resonators with more modes on a big chip ($4.3\ mm \cdot 9.3\ mm$) (Fig. 4.11). The simulation and the measurements fitted well (Fig. 4.16) with the previous fitting parameters (Tab. B.2). The resonances can be seen up to the 11^{th} mode (C0CE1) at 33 GHz and are still overcoupled ($g = 9$ for the first mode of C3CF2) .

Since the Rydberg atoms will fly crossways over the chip, we measured and simulated the microwave spectrum of a chip lying crossways in the PCB (Fig. 4.18). The resonators were coupled weaker than before. The measurements and simulation only matched for the resonances (Fig. 4.20 and Fig. 4.21). This is due to a) the small chip size and b) the curvature of the transmission line, that enhances coupling out of the waveguide. The fitting parameters are shown in Tab. B.2, which leads to a $g = 2$ (for the first mode of G1A1) and thus the resonators are still overcoupled.

The kinetic inductance plays an important role in superconducting NbTiN microwave resonances. For the geometry of the sample measured before at a temperature of 4.2 K the ratio of the kinetic to the magnetic inductance is 0.04 (Fig. 2.8). In order to increase this ratio, we a) changed the temperature of the chip and b) changed the geometry of the waveguide. The frequency shift was measured and simulated for temperatures between 8 and 13 K (Fig. 4.3.2). The raw theory and the measurement were quite similar. Changing the geometry led also to a shift in the resonance frequencies (section 4.3.1).

5.2 Overlook

The next step in the experiment is to measure chips with less coupling than G5A2/G1A2 (Tab. 4.1). For this a new mask was made. We want the samples to be strongly undercoupled to measure a high external Q-factor. This allows to determine the internal Q-factor more exact than for the sample of these experiments (Fig. 4.10, Fig. 4.17 and Fig. 4.21). On the new chips, the resonator extends over the curves. Since there are only selective modes in the resonator, we hope, that the curves have not such a strong influence on the transmission off-resonance.

The PCBs in the next experiment should fulfill the required geometry in order to get a better impedance match between the coaxial cables and the print MMPX-connectors (section 3.2 and Fig. 3.2).

The temperature dependance measurement (section 4.3.2) has only been performed for temperature higher than 4 K. While wring up this thesis a new setup is build, which a) allows to decrease the temperature of the

chip to 2.8 K and b) allows for finer temperature adjustment, in order to characterize the frequency shifts and the Q-factors at lower temperatures. The new setup is also expected to improve the measurement accuracy of the internal Q-factors.

5.3 Acknowledgments

I thank Prof. Andreas Wallraff for providing the laboratory work in the Quantum Device Lab. I also thank my supervisor Tobias Thiele for helping me in this six month and for his patience to answer my question. Furthermore I thank the whole Quantum Device Group for their kindness and their support in difficult situations. I also thank the staff of the FIRST laboratory, for providing their equipment and for helping out in difficult situations.

Bibliography

[1] Web: http://en.wikipedia.org/wiki/File:Bloch_sphere.svg , 2.11.2011

[2] Web: http://de.wikipedia.org/wiki/Shor-Algorithmus, 11.01.2012

[3] Weblink: http://en.wikipedia.org/wiki/Grover's_algorithm, 13.2.2012

[4] H. J. Kimble, The quantum internet, Nature 453, 2008

[5] D.F Walls and G.J. Milburn, Quanum optics, Springer-Verlag, Berlin, 1994

[6] Superconducting Solid State Cavity Quantum Electrodynamics, A. Wallraff, H. Majer, L. Frunzio, Rob Schoelkopf

[7] T. Gallagher, Rydberg atoms, Cambridge University Press, 1994

[8] E. Luc-Koenig and A. Bachelier, J. Phys. B **13**, 1743 (1980)

[9] M. L. Zimmerman, M. G. Littman, M. M. Kash, and D. Kleppner, Phys. Rev. A 20, 2251 (1979)

[10] Web: http://en.wikipedia.org/wiki/Wave_impedance

[11] Web: http://en.wikipedia.org/wiki/Waveguide_(electromagnetism)

[12] Web: http://websupplements.net/projects/virtual_labs/uploads/experiments/1295637311_exp6_coplanar_waveguide.png, 3.11.2011

[13] Coplarnar Waveguide Resonators for Circuit Quantum Electrodynamics, M. Goeppl et. al, 2008

[14] http://en.wikipedia.org/wiki/Superconductivity

[15] Kinetic Inductance of Superconducting Coplanar Waveguide, Koki Watanabe, Keijii Yoshida, Takeshi Aoki and Satoshi Kohjiro, Jpn. J. Appl. Phys. Vol. 33 (1994)

[16] Web: http://en.wikipedia.org/wiki/Niobium-titanium, 5.1.2012

[17] Weblink: http://www.mt-berlin.com/frames_cryst/descriptions/sapphire.htm, 12.2.2012

[18] Weblink: http://en.wikipedia.org/wiki/Loss_tangent, 12.2.2012

[19] Weblink: http://de.wikipedia.org/wiki/Fotolithografie_(Halbleitertechnik), 28.3.2011

[20] Characterization of Coplanar Waveguide Ringresonators for Circuit QED Applications, 2011

[21] FIRST Bonder Manual

[22] Master Thesis of S. Marx, December 2010

[23] Web: http://en.wikipedia.org/wiki/Four-terminal_sensing , 10.1.2012

[24] Manual for Model 325 Cryogenic Temperature Controller

[25] Manual for R&S ZVM, ZVK Vector Network Analyzers

[26] Web: http://www.compliance-engineering.com/wireless_services.htm, 10.1.2012

[27] Coaxial Assemblies and Coplanar Waveguides for Microwave signals up to 40 GHz, Meinrad Sidler (2010)

[28] Weblink: http://en.wikipedia.org/wiki/Propagation_of_uncertainty, 17.2.2012

[29] Weblink: http://www.microwaves101.com/encyclopedia/coaxloss.cfm, 8.4.2011

Appendix A

Additional Figures

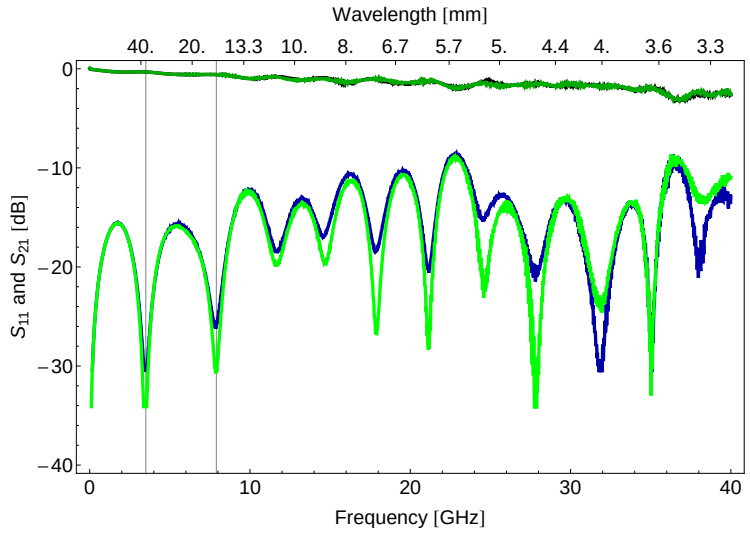

Figure A.1: The spectrum of a Type 1 PCB. The blue curve is S_{11}, the black curve is S_{12}, the dark green curve is S_{12} and the bright green curve is S_{22} of the waveguide. The black lines mark the frequency different $\Delta f = 4.4\ GHz$ ($\Delta\lambda = 29\ mm$) of the oscillations.

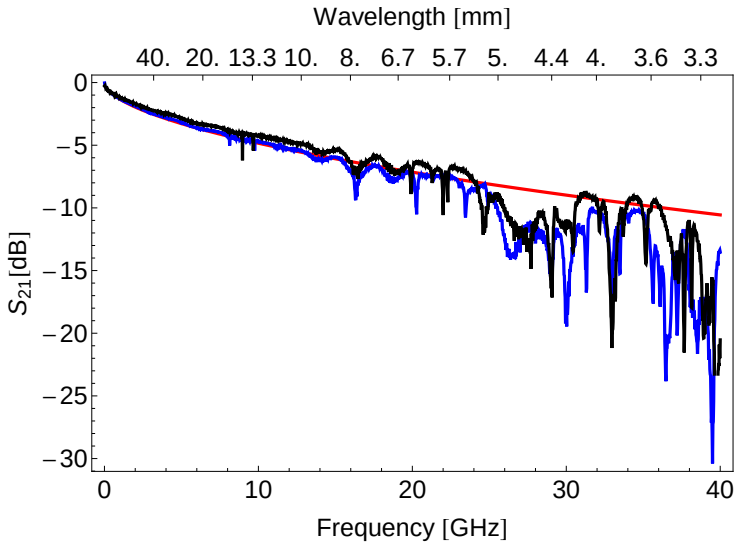

Figure A.2: The transmission of C5CD2 (blue) and the measured (black) and simulated (red) transmission of C5CD1.

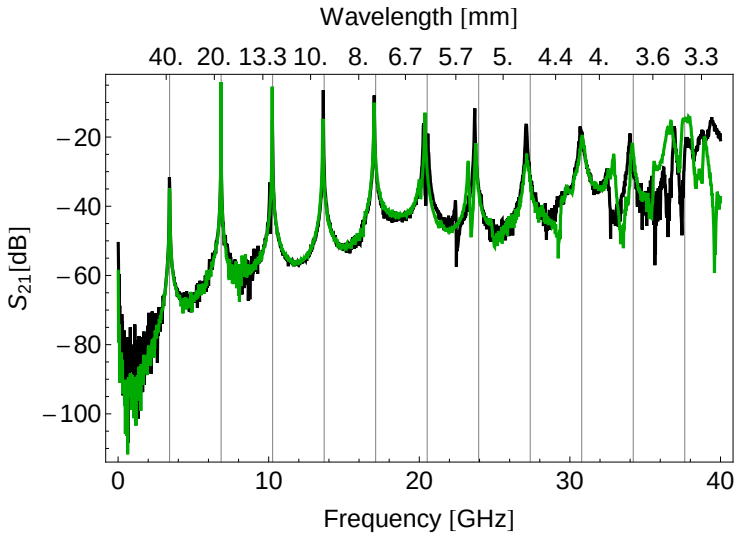

Figure A.3: Transmission and reflection spectrum of C1CF1(curved, small capacitance, black) and C3CF2 (curved, small capacitance, green). The two samples have the same geometry and look similar up to 34 GHz. The resonances are at the expected frequencies. The black, dotted lines show multiples of the ground mode frequency of 3.42 GHz.

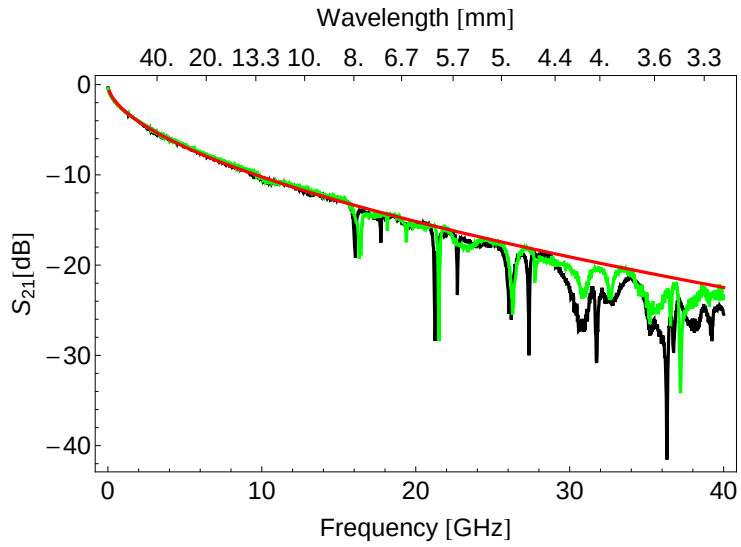

Figure A.4: The transmission of G3D1 (black) and G6D2 (green) are measured and fitted for G3D1(red) by $y(f) = -2.851 \cdot f^{0.5588507}$. The fitting curve match the data nearly perfect in the fitting range.

Appendix B

Tabulated Measuring Value

D0E1

f [GHz]	**α $[m^{-1}]$**	**Q_{int} meas. simulated**	**Q_{ext} meas. simulated**	**Q meas. simulated**
6.83965	-0.00947474	-23035.7 35862.1	246.132 236.927	248.79 235.372
13.6617	-0.0180943	-12062.2 17931.1	164.215 119.644	166.482 118.851
20.4986	-0.00278415	-78392.8 11954.	92.3168 81.0747	92.4256 80.5285
27.2305	0.11378	1918.24 8965.53	53.3333 62.1836	51.8906 61.7553
33.861	0.13513	1615.16 7172.42	89.5735 51.1638	84.867 50.8014

D4E1

f [GHz]	**α $[m^{-1}]$**	**Q_{int} meas. simulated**	**Q_{ext} meas. simulated**	**Q meas. simulated**
6.85938	0.0115494	18897.7 35862.1	260.434 242.628	256.894 240.997
13.7139	0.00565577	38590.2 17931.1	153.822 122.495	153.211 121.664
20.5659	0.0283152	7708.13 11954.	89.237 82.9751	88.2158 82.4032
27.354	0.319447	683.234 8965.53	60.2896 63.6089	55.4009 63.1608
34.1229	0.330539	660.306 7172.42	59.7636 52.3041	54.8034 51.9254

D7D1

f [GHz]	**α [m^{-1}]**	**Q_{int} meas. simulated**	**Q_{ext} meas. simulated**	**Q meas. simulated**
7.00566	0.0280659	7776.58 35629.6	1395.99 1328.63	1183.53 1280.87
14.0035	0.00811795	26885.7 17814.8	935.035 665.496	903.609 641.531
20.9717	0.0107487	20305.4 11876.5	581.37 444.976	565.188 428.906
27.8517	0.0385261	5665.17 8907.39	314.023 335.11	297.531 322.96
34.7855	0.0509491	4283.82 7125.91	466.392 269.505	420.6 259.683

O6D1

f [GHz]	**α [m^{-1}]**	**Q_{int} meas. simulated**	**Q_{ext} meas. simulated**	**Q meas. simulated**
6.99536	0.0267584	8156.57 35629.6	1383.03 1328.63	1182.52 1236.42
13.9888	0.020196	10807. 17814.8	952.185 665.496	875.083 619.232
20.8666	0.0312302	6988.66 11876.5	735.444 444.976	665.42 413.957
27.7786	0.145747	1497.51 8907.39	314.776 335.11	260.103 311.66
34.4059	0.160414	1360.58 7125.91	306.068 269.505	249.861 250.553

C0CE1

f [GHz]	**α $[m^{-1}]$**	**Q_{int} meas. simulated**	**Q_{ext} meas. simulated**	**Q meas. simulated**
3.37774	0.00386292	56500.5 74772.3	1115.57 1060.58	1093.97 1045.74
6.75469	0.00455976	47866. 37386.1	579.346 531.47	572.418 524.02
10.1553	0.0431499	5058.11 24924.1	424.752 355.625	391.847 350.622
13.4807	0.0215768	10115.4 18693.1	319.339 268.096	309.566 264.306
16.8751	0.182185	1198. 14954.5	187.007 215.894	161.757 212.822
20.1151	0.232307	939.521 12462.	216.28 181.355	175.809 178.754
23.454	0.222527	980.813 10681.8	152.79 156.909	132.197 154.637
26.8579	1.31438	166.053 9346.53	127.225 138.771	72.0345 136.741
30.6229	1.71927	126.947 8308.03	94.7939 124.839	54.2697 122.991
33.8354	1.15462	189.029 7477.23	176.285 113.851	91.2174 112.143
35.9651	0.744698	293.081 6797.48	82.5825 105.004	64.4283 103.406

C3CF2

f [GHz]	**α [m^{-1}]**	**Q_{int} meas. simulated**	**Q_{ext} meas. simulated**	**Q meas. simulated**
3.4206	0.00391864	55697.1 74772.3	6169.57 5848.78	5554.32 5424.47
6.83328	0.00414026	52715.8 37386.1	2798.97 2925.57	2657.85 2713.25
10.2325	0.011285	19340.5 24924.1	2253.94 1951.69	2018.68 1809.96
13.5958	0.0103091	21171.3 18693.1	1798.97 1465.15	1658.08 1358.66
17.0008	0.118141	1847.43 14954.5	921.648 1173.53	614.891 1088.14
20.3792	0.196431	1111.11 12462.	1027.82 979.389	533.922 908.027
23.7448	0.353112	618.097 10681.8	2056.63 840.938	475.262 779.566
27.1203	1.66713	130.918 9346.53	910.363 737.297	114.458 683.388
30.8275	1.45477	150.029 8308.03	430.72 656.862	111.271 608.733
34.1433	0.718077	303.947 7477.23	976.674 592.671	231.807 549.144
37.738	1.18981	183.439 6797.48	119.906 540.295	72.5096 500.512

C6CE2

f [GHz]	$\boldsymbol{\alpha}$ $[m^{-1}]$	$\mathbf{Q_{int}}$ **meas.** **simulated**	$\mathbf{Q_{ext}}$ **meas.** **simulated**	**Q meas.** **simulated**
3.37391	0.00560526	38937.9 74772.3	1244.77 1060.58	1206.21 1045.74
6.7341	0.00362289	60243.9 37386.1	677.956 531.47	670.412 524.02
10.0871	0.00966222	22588.7 24924.1	374.413 355.625	368.308 350.622
13.4369	0.000655501	332962. 18693.1	314.035 268.096	313.739 264.306
16.9101	0.970735	224.837 14954.5	330.489 215.894	133.806 212.822
20.0892	0.18391	1186.76 12462.	169.28 181.355	148.149 178.754
23.3378	0.226326	964.348 10681.8	243.443 156.909	194.375 154.637
26.8414	4.70356	46.4025 9346.53	171.148 138.771	36.5051 136.741
30.5002	2.64133	82.6317 8308.03	325.532 124.839	65.9031 122.991
33.5	0.999576	218.35 7477.23	1304.67 113.851	187.046 112.143
36.7441	0.802254	272.055 6797.48	309.915 105.004	144.877 103.406

C1CF1

f [GHz]	**α [m^{-1}]**	**Q_{int} meas. simulated**	**Q_{ext} meas. simulated**	**Q meas. simulated**
3.41737	0.0033027	66084.5 74782.2	5716.13 5849.17	5261.06 5424.86
6.83596	0.00614428	35522. 37391.1	2699.03 2925.77	2508.44 2713.44
10.2536	0.0598471	3646.91 24927.4	2501.79 1951.82	1483.86 1810.09
13.6281	0.00740549	29472.3 18695.5	1772.72 1465.24	1672.14 1358.75
17.0059	0.0629189	3468.86 14956.4	1063.41 1173.61	813.902 1088.22
20.2787	0.326249	668.989 12463.7	1371.8 979.453	449.688 908.091
23.6811	0.149528	1459.64 10683.2	1141.5 840.993	640.559 779.62
27.0934	0.381138	572.646 9347.77	801.22 737.345	333.959 683.436
30.7316	0.906488	240.772 8309.13	446.066 656.905	156.369 608.776
33.9817	0.672145	324.717 7478.22	842.951 592.71	234.416 549.182
36.9328	0.343047	636.231 6798.38	849.626 540.33	363.802 500.547

G2B1

f [GHz]	**α [m^{-1}]**	**Q_{int} meas. simulated**	**Q_{ext} meas. simulated**	**Q meas. simulated**
8.39255	0.0103291	21130.2 19921.6	3006.93 2484.72	2632.34 2209.18
16.7493	0.0125743	17357.4 9960.78	1470.13 1243.54	1355.34 1105.52
25.0448	0.066051	3304.37 6640.52	1920.16 830.339	1214.45 738.052
33.2788	0.15238	1432.33 4980.39	1092.05 624.132	619.627 554.627

G1A1

f [GHz]	**α $[m^{-1}]$**	**Q_{int} meas. simulated**	**Q_{ext} meas. simulated**	**Q meas. simulated**
8.3563	0.0111356	19599.9 18676.5	10637.2 9637.71	6895.12 6357.18
16.6624	0.0275188	7931.19 9338.23	3107.37 4820.04	2232.64 3179.1
24.8324	0.0791629	2757.06 6225.48	6277.14 3214.67	1915.66 2119.97
33.2069	3.1901	68.417 4669.11	2635.42 2412.38	66.6858 1590.58

G5A2

f [GHz]	**α $[m^{-1}]$**	**Q_{int} meas. simulated**	**Q_{ext} meas. simulated**	**Q meas. simulated**
8.36566	0.0508649	19794.1 18220.6	4290.92 3880.82	3526.46 3199.38
16.7311	0.0773019	30791.9 9111.48	2823.44 1940.41	2586.29 1599.73
24.8771	0.115715	1886.16 6075.63	74014.8 1293.61	1839.29 1066.53
33.6612	0.729641	5983.99 4558.1	299.13 970.205	284.888 799.937

E1B2

f [GHz]	**α $[m^{-1}]$**	**Q_{int} meas. simulated**	**Q_{ext} meas. simulated**	**Q meas. simulated**
8.3729	0.00796653	27396.7 19921.6	3142.62 3015.61	2819.23 2619.14
16.7709	0.549027	397.535 9960.78	418.493 1508.99	203.872 1310.46
25.0409	0.480443	454.283 6640.52	1310.98 1007.3	337.375 874.631
33.1562	0.470974	463.417 4980.39	2120.8 756.856	380.314 657.011

Table B.1: The measured resonance frequencies, measured attenuation constants and the measured and simulated Q-factors of the resonators used in these experiments.

Sample	$\mathbf{C}_\kappa[fF]$	$\boldsymbol{\alpha_2}$ $[\boldsymbol{m^{-1}s^2}]$	$\boldsymbol{\beta_0}$ $[\boldsymbol{m^{-1}}]$	$\boldsymbol{\beta_1}$ $[\boldsymbol{m^{-1}s}]$	$\mathbf{l}[\mu m]$
D4E2	25	0.0001	51.2	0	8636
D7D1	10.6	0.0001	51.46	0.006	8580
D0E1	25.3	0.0001	51.25	0.01	8636
O6D1	10.6	0.0002	51.535	0.0025	8580
C0CE1	24.9	0.0001	50.77	0	18006
C3CF2	10.6	0.0001	50.70	0.0169	17964
C6CE2	24.9	0.0001	50.72	0.031	18006
C1CF1	10.6	0.0001	50.80	-0.0025	17964
G2B1	6.5	0.00015	51.32	0.014	7196
G1A1	3.3	0.00016	51.79	0.019	7196
E1B2	5.9	0.00015	51.50	0.014	7196
G5A2	2.4	0.00077	51.973	0	7196

Table B.2: Properties of the NbTiN found by fitting the transmission spectrum. The Propagation constant is given by $\gamma = \alpha + i\beta$, where α is the attenuation constant ($\alpha = \alpha_0 \cdot f^2$) and β is the phase constant ($\beta = \beta_0 + \beta_1 \cdot f$)
.